UCLouvain

École polytechnique de Louvain

Degradation of biodegradable stents :

Evaluation and optimization of microCT for the characterization of the degradation rate and the roughness evolution

Author: **Ysaline Weinreb-Willard**
Supervisor: **Greet Kerckhofs**
Readers: **Pascal Jacques, Laurent Delannay**
Academic year 2019–2020
Master [120] in Biomedical Engineering

Acknowledgements

A number people have helped and supported me in writing this thesis. I want to thank them so much for that.

Firstly, I would like to express my gratitude to my promoter, Professor Greet Kerckhofs. Thank you for giving me the opportunity to write this master thesis. Thank you for your positive and effective supervision. Thank you for all your good advices and support throughout the year. Your contribution on some problems was key to complete this project successfully.

Secondly, I would like to thank PhD student Lisa Leyssens, my supervisor and daily contact. Thank you for your guidance, your close follow-up, your personal investment and all the good suggestions you proposed to me throughout the year. Special thanks for all the feedbacks you shared with after reviewing my work. Your role has been crucial in helping me deliver this master thesis.

Thirdly, I would like to thank Professor Pascal Jacques and Professor Laurent Delannoy for being part of my master thesis jury and for reading and evaluating my work.

My family has also helped in writing this master thesis and I am very much thankful to them. I would like to take this opportunity to also thank them for their continued support throughout my five years at university. They have always believed in me and encouraged me in difficult times.

Last but not least, special thanks for my friends who made it more pleasant for me to write this master thesis.

Abstract

Stent technology has been introduced in the 80s to overcome the limitations of balloon angioplasty. However, complications can still occur after the implantation of permanent metallic stents such as prolonged physical irritations, chronic inflammation, stent fracture, thombosis and particularly in-stent restenosis. Nowadays, to overcome those limitations, the most promising type of stents is the biodegradable stent. As the name suggests, the stent remains in situ only for a limited period of time before being completely degraded and disappearing, allowing reendothelialization to take place. So far, two main materials have been mostly investigated : magnesium-based alloys and iron-based alloys. This master thesis is focused on the latter. Pure iron shows adapted mechanical properties. However, its degradation is too low and need to be increased by alloying. TWIP was created to meet this need.

To select the best candidate material for biodegradable stent applications, a detailed characterization is required. In this master thesis, the degradation and roughness of pure iron and TWIP samples was analysed using different physical and microCT-based methods. Studying degradation and roughness of candidate materials for biodegradable stent applications and gathering a 3D reconstruction of the samples before and after immersion thanks to microCT is something that has not been done yet. Therefore, the use of microCT needs to be assessed and optimised for the characterization of the degradation rate and roughness evolution over time. For this purpose, the roughness and degradation rate of wires made of TWIP and pure iron was analysed during dynamic immersion tests.

Results highlighted the limitations of microCT to compute the degradation rate with the mass loss method. Several assumptions have been done to explain those bad results. An aliasing effect may occur at the ends of the scan, wires may be curved during degradation and handling, a protective layer may form on the surface or spatial image resolution may be too low to detect such small volume differences. Inductively coupled plasma mass spectrometry results has allowed us to observe an increase in the degradation rate of TWIP after 5 hours of immersion. For microCT-based roughness analysis, two different Matlab routines were used, both using linear baselines. The first one rapidly demonstrated limitations as it is not able to take into account the curvature of the wire. The second one gave better results. It enabled us to detect the presence of outliers. It showed an higher initial roughness for TWIP caused by the manufacturing process. It also allowed us to demonstrate a low correlation for both materials between the degradation rate and the initial roughness, meaning that alloying has effectively improved the corrosion rate of TWIP. Finally, we were able to observe the roughness evolution of pure Fe over time.

To conclude, the use of microCT seems limited to compute the degradation rate. Its use for roughness analysis seems more promising. However, additional work should be done to evaluate the roughness with polygonal baselines instead of linear baselines. Ideally, the roughness should be analysed with a routine that could compute the roughness parameters in 3D, taking into account any outliers. Comparison should also be made between microCT and standard profile measuring systems results. Finally, no conclusion could be drawn concerning the use of TWIP for biodegradable stent applications since the number of samples was limited and its roughness and degradation rate evolution over time could not be observed.

Contents

List of Figures

List of Tables

List of abbreviations

AC Alternating current

CE Counter electrode

CE-CT Contrast-enhanced microCT

CFD Computational fluid dynamics

CHD Coronary heart disease

CR Corrosion rate

CVD Cardiovascular disease

DMEM Dulbecco/Vogt modified Eagle's minimal essential medium

ECM Extracellular matrix

ED Endothelial dysfunction

EIS Electrochemical impedance spectroscopy

HCY Homocysteine

HDL High density lipoprotein

hs-CRP High-sensitivity C-reactive protein

ICP Inductively coupled plasma

ICP-MS Inductively coupled plasma mass spectrometry

ISR In-stent restenosis

IVUS Intravascular ultrasound

LDL Low density lipoprotein

LDLR Low density lipoprotein receptor

microCT High-resolution microfocus X-ray computed tomography

NO Nitric oxide

OCP Open circuit potential

PBS Phosphate buffered saline

PCI Percutaneous coronary intervention

RE Reference electrode

RF Radio frequency

ROI Region of interest

ROS Reactive oxygen species

SBF Simulated body fluid

ST Stent thrombosis

VBT Vascular brachytherapy

VH-IVUS Virtual histology intravascular ultrasound

VSMC Vascular smooth muscle cell

WE Working electrode

Part I
Introduction

According to the World Health Organization, an estimated 17.9 million people died from cardiovascular diseases (CVDs) in 2016, representing 31% of all global deaths and making them the leading cause of death for the world population [1]. Of these deaths, 85% are due to heart attacks and strokes, both considered as coronary heart diseases (CHDs) also called ischemic heart diseases. Ischemia can be defined as inadequate blood supply to a local area due to blockage of the blood vessels supplying that area. The most common cause for this is a build-up of plaque, called atherosclerosis, on the inner walls of the veins or arteries [2]. If left untreated, the plaque can become vulnerable and could potentially break out. A blood clot called thrombus can be created by the body's immune system in reaction to the injury. This clot can block an artery, leading to either a heart attack or stroke [3]. When blood vessels are narrowed by plaque, stents can be used to allow an adequate oxygen-rich blood flow. Indeed, the stent keeps the narrowed arteries open and therefore, allow for an adequate blood flow. Stents are also sometimes used to treat the aorta if it has an aneurysm or bulge in it [4].

The problem is that stents do not last for ever. Stent technology continues to be associated with complications including restenosis and thrombosis [5]. Indeed, even if the cases of restenosis have considerably decreased thanks to stenting following angioplasty, in about 25% of stenting cases, complications related to restenosis can still occur [6]. We then speak of in-stent restenosis. Several different techniques and treatments have been implemented in order to treat in-stent restenosis. Repeated balloon angioplasty alone has been rapidly followed by ablative techniques such as laser or rotational atherectomy. Deploying of a second stent within the stent represents another effective alternative technique as well as cutting balloon. None of these techniques has proven its superiority over balloon angioplasty alone. The only effective technology that can significantly reduce the rate of restenosis at follow-up is called vascular brachytherapy. However, its use was quickly limited by the cost, associated infrastructures and the risk of late thrombosis requiring extended antiplatelet therapy. Surgical treatment as well as medical therapy can also be proposed in recurrent in-stent restenosis. In any case, the patient will always have to bear costs and face risks [7].

In order to minimise the amount of complications and consequently the money and time lost by patients and the risks involved, a solution has to be found. This master thesis is part of a broader research project aimed at developing a biodegradable metallic stent. The main purpose of this work is to assess and optimise the use of microCT for biodegradable stents characterization. To do so, the *in vitro* corrosion rate and roughness of TWIP (Fe-Mn-Al-Si) and pure iron will be analysed after *in vitro* immersion using physical and microCT-based methods. It is known that the degradation process and the roughness have an influence on the in-stent restenosis rate upon implantation of the stent. Moreover, the degradation rate should be adapted and the stent should disappear timely. Therefore, data collected *in vitro* need to be properly characterized to better understand the transformations that the stent will undergo *in vivo* and therefore give insights on the possible use of TWIP as an appropriate material for biodegradable stent technology.

Part II
State of the art

1 Cardiovascular system

The cardiovascular system is composed of the heart, which acts like a blood pump, and the network of vessels, which brings blood to the different organs of the body and brings it back to the heart where it can be re-oxygenated by the lungs. A relatively high pressure allows blood to be ejected from the heart. It then flows through the main arteries. Gradually, the network branches out and the blood joins the arterioles and finally the capillaries, where oxygen and several nutrients are delivered to the various organs and where carbon dioxide and catabolites are removed. Blood returns to the heart through a network of veins and at a lower pressure [8]. A system of valves in the veins allows to prevent backflow. Although arteries and veins have many structural and functional differences, they also share many common characteristics (Figure 1).

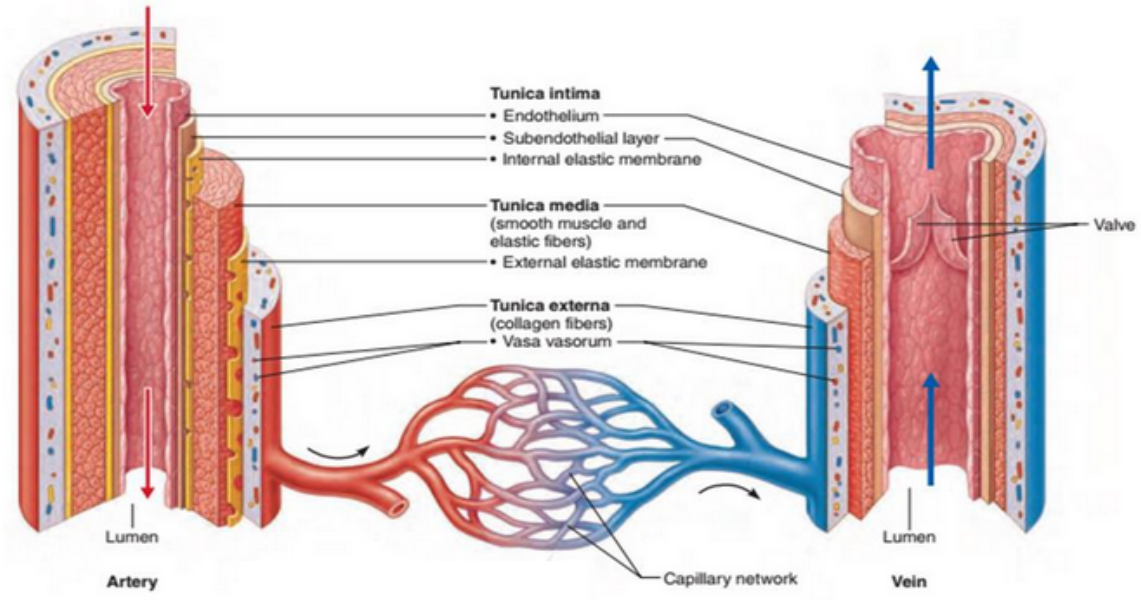

Figure 1: Blood vessels anatomy (veins and arteries). Adapted from [9]

A healthy blood vessel wall is composed of three different layers : the tunica intima, the tunica media and the tunica externa. The tunica intima is the thinnest and innermost layer. It mainly consists of endothelial cells, which form a continuous monolayer covering all blood vessels. Only their structure or function can vary depending on their location in the vascular tree. However, they all have three things in common in their resting state. They are thrombogenic and, therefore, allow the blood to remain in its fluid state. They have an important role in the delivery of nutrients to the subendothelial structures. And, finally, they also prevent a certain permeability to cells, macromolecules and to the particles that circulate in the blood by acting as barriers. This permeability can vary under some specific conditions and, thus, allow the passage of various molecules and cells. The intima tunica is also made of a small amount of subendothelial connective tissue and,

in some larger arteries, of a thick and distinct layer composed of elastic fibers called the internal elastic membrane. This layer forms a border with the tunica media [10]. The tunica media acts as a structural support and provides vasoreactivity and elasticity to the blood vessels. It consists of smooth muscle cells and connective tissue, the amount of which depends on the type of vessel. Again, an elastic membrane, called the external elastic membrane, separates the tunica media from the tunica externa. This structure is generally only present in the major arteries. The tunica externa is the outermost layer and is entirely made up of fibrous connective tissue such as collagen fibers. The purpose of collagen is to anchor blood vessels to nearby organs, giving them stability. It also contains the nerves of the vessel and nutrient capillaries (vasa vasorum) in large blood vessels. The internal and hollow region of the vessel is called the vessel lumen [11].

2 Atherosclerosis

Atherosclerosis is an inflammatory disease characterized by the narrowing of the arteries due to the build-up of a modified fatty deposit (Figure 2). A severe inflammatory response generally follows the accumulation of lipids and is characterized by the formation of atherosclerotic plaques. Several specific cells are involved in the process: inflamed smooth muscle cells, endothelial cells, foam cells, leukocytes, macrophages, dendritic cells, lymphocytes and other inflammatory cells. Many studies report that the risk factors for atherosclerosis are closely related to physical injury due to stenting, stress caused by hypertension or turbulent blood flow, hyperlipidemia (high blood concentrations of low density lipoproteins (LDLs)) or an increase in the production of reactive oxygen species (ROS). This results in endothelial dysfunction and oxidation of LDLs, followed by an inflammatory response, all contributing to the pathogenesis of atherosclerosis [12].

A dynamic and active interface between the blood flow and the vessel wall is provided by the endothelial cells. The endothelial cells monolayer acts as a semi-permeable barrier allowing the potential entry of certain fluids, nutrients, gases and waste to the tissues from the blood. The first step in the pathophysiology of atherosclerosis is characterized by an endothelial dysfunction (ED). Damages to the endothelium is the cause of the inhibition of the production of nitric oxide (NO) known to be a powerful vasodilator. Damages also stimulate the production of adhesion molecules [13]. These molecules attract inflammatory cells to the arterial wall where monocytes can go through. They then migrate to the intima tunica, where they differentiate into macrophages [12].

Blood cholesterol levels are well balanced and highly regulated under normal healthy conditions. LDL is known to be an essential lipoprotein. They can indeed enable the transport of cholesterol between the liver and the rest of the tissues. They are then incorporated into the tissue cells by receptor-mediated endocytosis via the LDL receptor (LDLR). High density lipoproteins (HDLs) allow the transport of excess cholesterol from the peripheral tissues back to the liver. As a result, the balance of metabolism is well maintained [12]. When ED occurs, one of the earliest changes is also seen in the permeability of the endothelium. Increased amounts of lipoproteins are transported through the endothelium to the sub-endothelial space of the tunica intima [14]. Oxidation of LDLs to oxLDLs occurs because of oxidative stress environments. Macrophages can easily engulf oxLDLs and an inflammatory response is then triggered, stimulating the production

of proinflammatory cytokines [12]. Macrophages then slowly turn into large foam cells forming the fatty streak [14].

The last stage of the disease is characterized by the apoptosis and necrosis of the foam cells accumulated in the arterial wall. This brings about the release of their fatty content and the formation of a necrotic core, which is rich in lipids. Furthermore, vascular smooth muscle cells (VSCMs) begin to proliferate under the influence of cytokines and growth factors. They then migrate from the tunica media to the tunica intima and form a fibrous cap around the lipid core. VSMCs also have an extracellular matrix (ECM), which strengthens the fibrous cap. Under normal healthy conditions, this smooth muscle proliferation can be prevented by the release of NO, but because of ED, the NO production is inhibited. VSMCs are also responsible for the production of collagen. However, under these above conditions, collagen is degraded by matrix metalloproteinases released by the inflamed macrophages in the necrotic core. Collagen production is also reduced by death or loss of function of the VSMCs. Finally, the rupture of the atherosclerotic plaque can occur. In this case, platelets aggregation happens quickly, a blood clot called thrombus can be formed and the arterial blood flow can be obstructed [12].

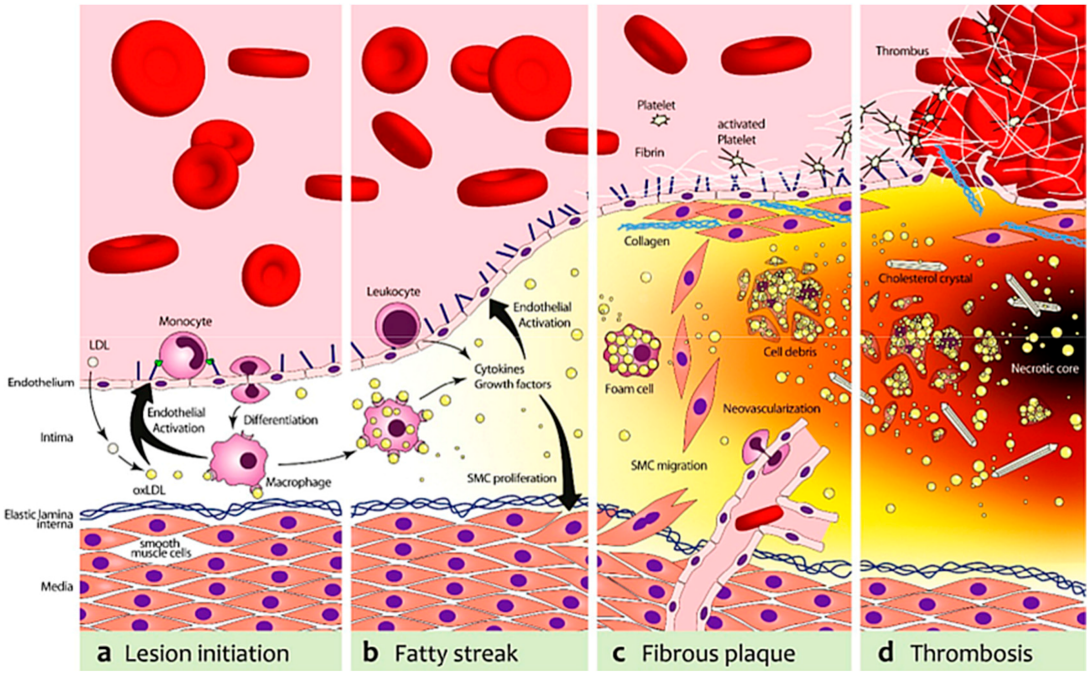

Figure 2: Atherosclerosis and plaque vulnerability. (a) ED results in an inflammatory response and monocytes enter the artery wall from the bloodstream and migrate to the intima of the arteries. Then, they differentiate into macrophages. LDL are deposited in the endothelium and undergo oxidative modification, resulting in oxLDL. (b) OxLDL are easily captured by macrophages forming a fatty streak, triggering an inflammatory response in the neighboring endothelial cells and stimulating the production of proinflammatory cytokines. (c) Macrophages slowly turn into large foam cells. Foam cells can undergo apoptosis and necrosis leading to the release of their fatty contents forming a necrotic core rich in lipids. VSMCs proliferate and migrate from the media to the intima of arteries forming a fibrous cap around the lipid core to stabilize the fibrous plaque. The increasing plaque volume promotes neovascularization. (d) Plaque rupture can occur followed by thrombotic events [15].

3 Possible treatments of atherosclerosis

3.1 Balloon angioplasty

Balloon angioplasty is a procedure used to open blocked arteries (Figure 3). Therefore, balloon angioplasty is a technique for restoring the blood flow. No open-heart surgeries are required. The process begins with the delivery of a balloon where the narrowed vessel is located. This is done with a catheter inserted in a peripheral artery, usually the femoral or radial artery. An appropriate pressure allows to inflate the balloon which will then expand the vessel, restoring the lumen size and improving the blood flow previously decreased [16].

However, acute vessel closure or elastic recoil in the short term and restenosis in the long term can happen, which highly limit the efficiency of the procedure. Moreover, the dilatation of the balloon can cause a severe injury to the artery. In response, the immune system reacts and restenosis can occur. To deal with those complications, stent technology was introduced in the 80s [16].

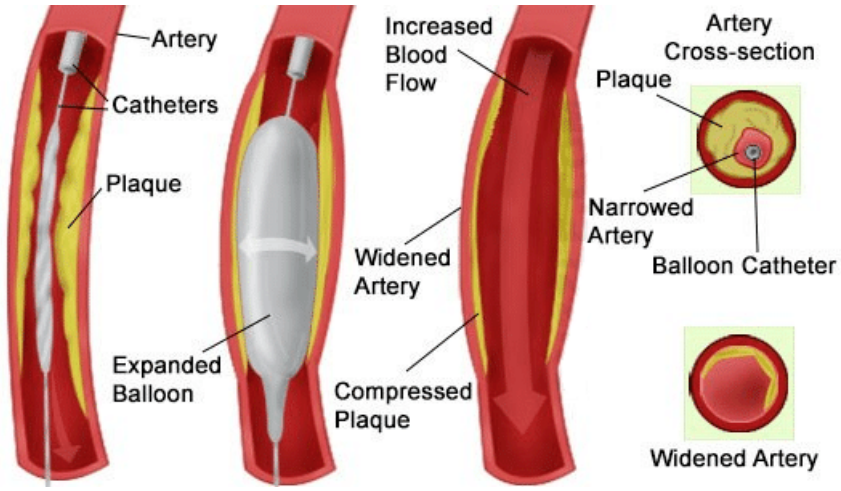

Figure 3: Balloon angioplasty procedure [17].

3.2 Stent technology

Nowadays, treatment of CVDs can be done using a well-established and minimally invasive technique, referred to as stenting [18]. Conventionally, a stent is a small tubular scaffold that can be inserted in narrowed vessels that are blocked by atherosclerosotic plaque to keep them open. It is usually made of medical-grade and corrosion resistant stainless steel, titanium or a cobalt-chromium alloy. The stent stays at the implantation site, which allows for the reduction of the obstruction and the prevention of the vessel narrowing [19]. At present, in about 60% of balloon angioplasties, the use of a stent is needed. When stenting is coupled with balloon angioplasty, the stent is positioned and expanded by the inflation of the balloon, which opens the stent and pushes it against the arterial wall. The balloon is then deflated, leaving only the stent in the artery and keeping it open (Figure 4) [6]. Mechanical support is then provided by the stent. Millions are implanted each year worldwide [18].

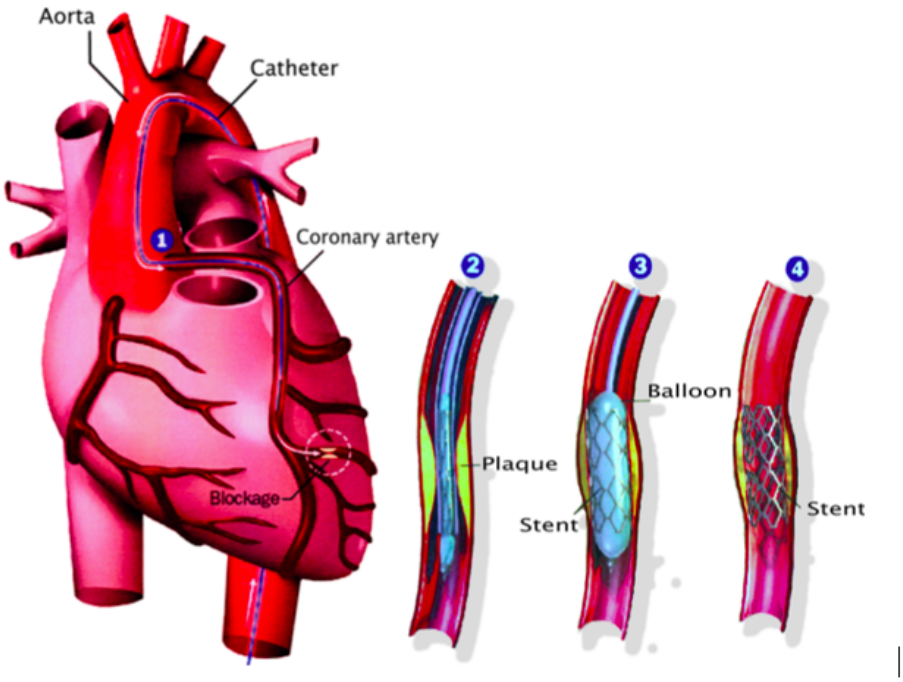

Figure 4: Schematic diagram of stenting representating the process of opening a blocked artery. (1) A catheter is inserted into a partially blocked artery. A dye can be released to locate the site of blockage. (2) A stent with a balloon is placed in the location of the plaque. (3) The inflation of the balloon causes the stent to expand. (4) The balloon is deflated and removed leaving the stent alone. The artery is kept open by the stent [19].

Since their first implantation in the 80s, cardiovascular stents have been designed to last. They are mainly made with materials such as 316L stainless steel or titanium and cobalt-chromium alloys. Those materials are known for their high strength, good biological performance, ductility and good corrosion resistance, making them the main materials used for medical implants. However, complications can occur after the implantation of permanent metallic stents such as prolonged physical irritations, chronic inflammation, stent fracture, thombosis and particularly in-stent restenosis (ISR) [19].

4 In-stent Restenosis

Still today, the precise mechanisms underlying ISR are not fully understood. However, it is known that the expansion and placement of the stent can cause an injury to the arterial wall. In response to this injury, the immune system will be activated. ISR is considered as a distortion of the natural healing response (Figure 5). The injury triggers a number of events, leading to the development of a neointima. The latter is composed of VSMCs and components from the extracellular matrix.

Generally, platelets are activated first and adhere to the stent struts. This is followed by the recruitment and activation of neutrophils, monocytes and macrophages within the thrombus. These events take place during the first week or so. This immune response releases a cocktail of cytokines and growth factors. This cocktail, and the injury caused by the stent deployment, bring about the activation of VSMCs, which then proliferate and

migrate towards the lumen. ECM is produced by the VSMCs and togheter they induce the neointima formation, which is characteristic of ISR [16].

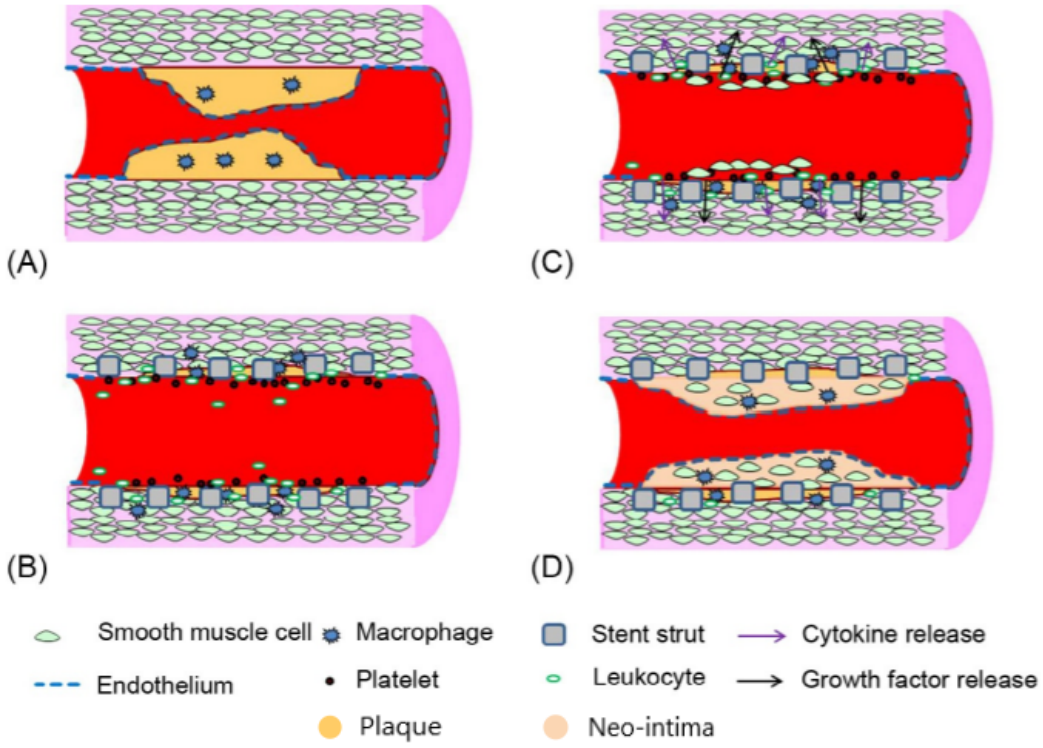

Figure 5: Schematic overview of ISR, showing key responses to stent implantation within a diseased artery. (A) Diseased artery with lumen narrowed by the presence of atherosclerotic plaque. (B) Stent implantation causes severe injury to the vessel wall, resulting in platelet adhesion/activation and recruitment and activation of neutrophils, monocytes, and macrophages. (C) Release of cytokines and growth factors triggers VSMCs to proliferate and migrate towards the lumen. (D) Mature neointima is formed, comprising VSCMs and ECM, covered by a restored endothelium. Adapted from [16].

When ISR occurs, repeated revascularization is necessary to treat previously stented atherosclerotic lesions. However, this procedure is complex and the fact that there are so many of them is the evidence that ISR still represents a significant clinical problem. Consequently, many studies have been carried out in order to develop strategies for preventing ISR and limiting the need for repeated revascularizations. [16]. For this purpose, a detailed characterization is required.

4.1 Characterization of ISR

4.1.1 Histology

Histology is the study of the microanatomy and the structure of biological material. It helps to assess the correlation between structure and function of the tissue as well as the relationship between individual components. Histology is a mixture of biochemistry, molecular biology and physiology, on the one hand, and pathological processes and their

effects on the other. It, therefore, represents a central tool used in biological and biomedical science. Knowledge of the histological aspects of healthy structures is essential to recognize diseased structures and to analyze and understand the biochemical and physiological processes behind them [20].

The extent of ISR has quite often been assessed by histological analyses. Histology has indeed been used to find a certain correlation between the neointimal formation on the one hand and the arterial lesion caused by the deployment of the stent and the characteristics (such as the number and distribution of the spacers, the type of stent, length, characterization of the surface and materials) of the stent on the other hand [21]. However, histology has some disadvantages. Since autopsy samples are used for the analysis, its usage remains limited by the number of specimens that is particularly low for humans. As a result, this limits the understanding of the vascular reaction to implantation of a stent through histology. In addition, the separation of metal and injured tissue without disturbing the tissue morphology represents a significant challenge. There is a technique which allows the stent to be removed before histological treatment. However, this method can cause the deterioration of the normal vascular architecture, in particular at the interface between the stent and the tissue [22].

4.1.2 Intravascular ultrasound

Based on information derived from histology, a technique called virtual histology intravascular ultrasound (VH-IVUS) can be used to detect the first signs of ISR. Intravascular ultrasound (IVUS) is generally used in clinical practice, but it only analyses the amplitude of the reflected ultrasound signals. Therefore, the assessment of the plaque composition is limited. Spectrum analysis of IVUS-derived radio frequency (RF) data allows for a more detailed analysis of the composition and morphology of the atherosclerotic plaque. This can be done using preliminary *in vitro* studies where the histological components of the plaque are correlated with specific spectrum analysis of the RF data. The different components (fibrous, fibro-fatty, necrotic core and dense calcium) are then associated to a specific color. Cardiovascular tissue maps can finally be reconstructed from RF data [23].

4.1.3 MicroCT and CE-CT

High-resolution microfocus X-ray computed tomography (microCT) is a technique for preclinical vascular imaging, enabling a resolution of the order of a micron. It is a non-destructive tomography technique used to reconstruct three-dimensional images of small and radiopaque pathological samples. One of the main advantages is that the specimens are kept intact allowing, for subsequent staining and histological analysis. Depending on the protocol and on the scanner, resolutions ranging from 0.5 to 100 micron voxels can be expected [24].

The use of microCT by vascular biologists has greatly increased for the study of angiogenesis, neovascularization, tumors as well as the morphology of the stented arteries and more particularly, the interaction between the stent and the arterial wall [24, 25, 26, 27]. After various types of fatigue testing, microCT is able to assess the stent design and integrity. However, microCT technolgy remains very limited by the maximum size of the sample that can be scanned (approximately $2 \times 2 \times 7$ cm corresponding to the size of

an adult mouse), which makes it impossible to use it for *in vivo* human imaging [24]. Another disadvantage of microCT is the inherently poor contrast in standard absorption mode which makes the visualization of soft biological tissues challenging.

Recently, the interest in contrast-enhanced microCT (CE-CT) has increased [28, 29]. Whole tissue samples are incubated in contrast agents allowing visualization of the soft tissues, such as muscles and adipocytes [29]. Indeed, to achieve sufficient X-ray attenuation, staining agents containing high atomic number molecules are adopted. CE-CT is a highly promising technique for full 3D visualization of the different subtissues within normal and diseased biological tissues. The effects of a disease on the tissue microstructure can be better understood.

4.1.4 Computer simulations

Computational fluid dynamics (CFD) looks at fluid movements and their effects by numerically solving the equations governing the fluid. This technology is then able to make predictions and to analyse fluid flow phenomena [30]. CFD can therefore be used to better understand and study the macro and micro aspects of the blood flow in blood vessels when it is affected by stents or atherosclerosis [31, 32]. Therefore, it allows to gain a better understanding of their influence on the neointima formation. It has indeed been proven that a value of shear stress lower than 0.5 Pa could be an important risk factor for ISR. CDF simulations also have drawbacks. Its use is limited to idealized deployed stents having a high degree of symmetry and uniformity. However, in reality, the numerous irregularities of the deployed stents have a significant impact on the hemodynamics. Therefore, simulations do not always reflect the *in vivo* influence of stents on the blood flow [21].

4.2 Parameters affecting ISR

Complications and adverse events, strongly influencing morbidity and mortality after stenting, are still present despite many advances in stent design and even more advanced pharmacological strategies. Therefore, preventing ISR by controlling the factors that have an influence on it represents today an urgent need and a major challenge [33].

This section gives an overview on some parameters that could have an impact on ISR and on how they could be controlled to avoid or mitigate ISR.

4.2.1 High-sensitivity C-reactive Protein (hs-CRP)

hs-CRP is considered as the most powerful inflammatory marker of cardiovascular or cerebrovascular diseases, and is known to be an inflammatory mediator of atherosclerosis. Post-operative inflammation can increase the instability of atherosclerotic plaques and lead to the formation of a blood clot and hypercoability [34]. Therefore the control of the inflammatory response is essential and can be done by correctly controlling the level of post-interventional hs-CRP level. Also, it has been proven that a higher hs-CRP level before the operation can have an influence on ISR compared with patients with a normal hs-CRP level [34, 35]. Thus, determination of the pre-interventional as well as the control of post-interventional hs-CRP level may help control the development of restenosis after stenting [34].

4.2.2 Homocysteine (HCY)

HCY is an intermediary amino acid formed by the conversion of methionine to cysteine. A high level of HCY can have a direct or indirect effect on the gene expression of vascular endothelial cells and a toxic effect that can lead to cellular apoptosis. In reaction, VSMCs will proliferate, migrate and lead to the formation of a fibrous cap and to the thickening of the arterial wall and therefore to the narrowing of the lumen size of blood vessels. The arterial elasticity is also modified and finally the formation of atherosclerotic plaques occurs [34]. De *et al.* have demonstrated that patients with moderately or severely elevated HCY levels may be at higher risk for restenosis and subacute thrombosis after stenting [36]. Therefore, monitoring the level of post-interventional, but also pre-interventional HCY can be useful in preventing ISR. This can be done with early intervention for hyperhomocysteinemia [34].

4.2.3 Diabetes

Diabetes is a disease known to have a significant influence and to be an independent risk factor for restenosis after stenting. Indeed, diabetic patients generally have long-term hypercoagulability, an endothelial vascular metabolism and a higher dysfunction of the blood flow which make those patients more prone to thrombosis. Certain growth factors responsible for intimal hyperplasia, proliferation and migration of VSCMs towards the lumen as well as the deposit of their ECM can be stimulated by insulin. An abnormal production of insulin can, therefore, have an impact on the formation of the neointima. Hence, glycemic control is, for these patients, essential to prevent a high rate of restenosis after stenting [34].

4.2.4 Lesion characteristics

Bifurcation lesions can induce a more complicated surgical process. In this case, the number of dilatations of the balloon on the arterial wall can be high . These repeated actions can increase the damage to the arterial wall and therefore deteriorate ED. This increases the rate of restenosis after stenting [34].

The length of the lesions is also recognized to be a risk factor for ISR. The more diffuse the lesions (> 10 mm), the higher the incidence of restenosis. ISR is also more common in small vessels [37].

4.2.5 Stent characteristics

The longer the stent, the more severe the injury to the arterial wall and the subsequent inflammatory response will be. Therefore, the size of the stent is also a parameter that can influence ISR. Appropriate stent expansion is also essential. An underexpansion or an overexpansion are two risk factors for ISR. Therefore, before stent insertion, it can be helpful to accurately estimate the length of the lesion and the diameter of the vessel. This way, the stent can properly cover the lesion and be placed correctly [34].

In addition, other characteristics of the stent, such as strut dimensions, strut profile (square, circular, elliptic, ortear drop), orientation and angle with respect to flow direction affect the flow pattern, and hence the distribution of hemodynamic forces inside the

stented artery. Numerous clinical investigations suggest that non-constant hemodynamic forces acting on the artery wall during the cardiac cycle may have an influence on neointima formation and therefore on ISR [21].

Also, surface topography is considered to have an important influence on stent performance. While smooth surface stents were previously associated with reduced thrombogenicity and neointimal proliferation, more recent experimental studies have suggested that stents with a previously treated rough surface may accelerate endothelialization of the stent, a process that has been associated with less thrombus formation and neointimal growth after stenting. The storage capacity of anti-restenotic drugs can also be improved thanks to the roughness present on the surface of the stent. The use of a polymer coating, which is often associated with a greater inflammatory response, is then no longer necessary [38]. In addition, a precise evaluation of the surface roughness can help analyse the local mechanical and dynamic properties of fluids, which are known to have some influence on ISR [39]. Finally, roughness can have a significant influence on the degradation rate in case of biodegradable stent. However, the influence of surface roughness on the corrosion property is usually ignored [40]. Therefore, controlling the roughness of the stent is crucial to avoid ISR.

Finally, many enhancements with regard to stent technology have been achieved to decrease the ISR rate. In 2001, to mitigate or avoid ISR, the concept of drug eluting stents (DES) was introduced. This technology slowly releases a drug that will limit cell proliferation and prevent the formation of a fibrous cap. However, several case studies and clinical investigations have shown that this technology is often associated with a high rate of stent thrombosis (ST) occuring unusually late. This is a phenomenon referred to as very late ST [41]. The goal is then to prevent ISR on the one hand and to avoid ST by accelerating the healing process and by promoting reendothelialization of the blood vessel on the other hand. Nowadays, the most promising type of stents for this is the biodegradable stent. As the name suggests, the stent remains in situ only for a limited period of time before being completely degraded and disappearing, allowing reendothelialization to take place. This period must be long enough to allow the widening of the vessel and avoid elastic recoil and constrictive remodeling [42]. This will be explained in more details in the section 5 of this chapter.

4.3 ISR treatments

4.3.1 Balloon angioplasty

Balloon angioplasty is one of the earliest treatments that has been used for patients with ISR. The procedure is technically straightforward and is explained in Section 3.1. The results associated with this treatment are most often satisfactory. In addition, it results in a very low incidence of complications. Axial and longitudinal tissue extrusion, as well as additional expansion of the stent, are responsible for the good results after balloon angioplasty. However, in some cases and within minutes after the last inflation of the balloon catheter, a reintrusion of the subacute tissue toward the lumen may occur. This may, in turn, limit the use of balloon angioplasty for the treatment of ISR [43].

4.3.2 Cutting balloon

The cutting balloon is an attractive and simple technique for the treatment of ISR. The balloon catheter has three or four atherotomes (microsurgical blades) on its surface. This makes it possible to create discrete longitudinal incisions in the atherosclerotic plaque of the target cardiovascular segment. It allows to avoid the sliding of the balloon and problems associated with it [44]. In addition, deep incisions of the neointimal tissue could ease its latter extrusion [45]. Consequently, this technique allows for a more controlled extension of the lumen of the vessels since a lower pressure is necessary for the inflation of the balloon than for conventional balloon angioplasty. The dilation is better controlled, which reduces the extent of lesions on the vascular wall and therefore decreases the rate of future ISR [44].

4.3.3 Ablative techniques

Because the long-term results of balloon angioplasty alone are often poor, new ablative techniques such as rotational atherectomy and excimer laser have been advocated. The use of laser or rotary atherectomy can be implemented after conventional balloon angioplasty, resulting in a decrease in ISR [46]. Both techniques involve physical removal of the neointimal tissue or the atherosclerotic plaque [43].

4.3.4 Vascular brachytherapy

Vascular brachytherapy (VBT) is a technique that is no longer used today but was one of the most promising treatment options at the time for patients with neointimal hyperplasia and ISR. In this technology, a radioactive isotope is temporarily placed in the diseased vascular segment. Clinical trials have shown that this technique can prevent the progression of ISR and dramatically reduce the rate of ISR. It can improve the results observed after balloon angioplasty alone or ablative procedures with excimer laser or atherectomy [43]. However, this technique can induce a fairly high rate of late restenosis and many logistical problems are related to the technology. This is why the use of VBT has decreased sharply in recent years, so that most hospitals no longer even have the devices necessary for the technology [47].

5 Biodegradable stents

Stenting is performed when remodelling of the arterial wall and widening of the vessel lumen are needed. This is possible thanks to the mechanical forces imposed by the stent deployed on the wall. However, a long-term presence of the stent is not necessary. After a while, the arterial tissue heals and finds a new equilibrium after being stressed by the deployment of the stent. Most of the problems encountered, such as ISR, late ST and the need for prolonged antiplatelet therapy when inserting a stent, are long term issues and, therefore, the use of a biodegradable stent could help avoid them [48].

An ideal biodegradable stent should be able to coordinate its degradation and mechanical integrity during implantation, as shown in Figure 6. Ideally, the stent should first be able to degrade very slowly and maintain its mechanical properties intact to provide the support needed to remodel the arterial wall. A period of 6 to 12 months should be

sufficient for complete healing of the cardiovascular wall. Then, when the mechanical properties of the stent start decreasing, it must degrade at a sufficient rate. Degradation should not result in an intolerable accumulation of the degradation products around the implantation site or the formation of toxic products for cells [48]. Degradation should also be uniform. Corrosion that is too localized on the stent can cause an undesirable implant failure. If this happens in the first days of implantation, when the wall is not yet completely remodeled, it can be particularly dangerous [49]. In total, a period of 12 to 24 months is considered reasonable for the stent before being completely degraded [48].

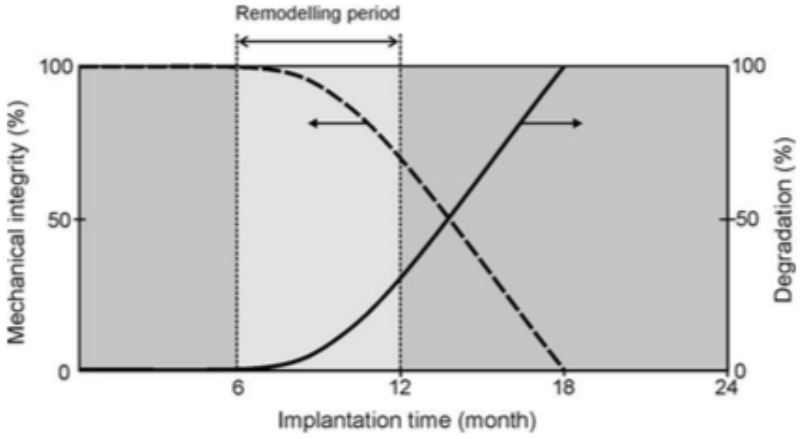

Figure 6: Illustration of an ideal compromise between mechanical integrity and degradation of a biodegradable stent [48].

The choice of material for this type of technology is crucial. Indeed, the mechanical properties and the rate of degradation depend on the implantation site and even more on the choice of the material. Therefore, design and development of stent materials with appropriate mechanical and degradation properties are key steps in the development of this new class of medical devices. Before performing *in vivo* studies, *in vitro* studies are essential to select potential candidate materials [48].

The candidate materials for such an application should have mechanical properties ideally close to those of 316L stainless steel (Table 1), which is today the most used material for permanent stents. These mechanical properties are adapted to provide sufficient support for diseased arteries [6]. Indeed, complications and damages to the cardiovascular wall can occur if the mechanical properties of the material used are not suitable for the technology. Also, when the material degrades, the degradation products are absorbed by the surrounding cells and by the blood. Therefore, these products should be non-toxic.

As a result of this, the material for biodegradable stents should have at least the following characteristics : it must be biocompatible; degradation products of the material must also be non-toxic and biocompatible; the material must stay in place for several months before its complete degradation and bioabsorption and the radial force of the stent must be sufficient to offer an adapted scaffolding effect during the requested period [6]. Properties of the ideal biodegradable cardiovascular stent are summarized in Table 2.

The two main materials investigated for biodegradable stents are polymers and metals.

Table 1: Mechanical Properties of 316L Stainless Steel as a stent material. [50, 51, 52]

Mechanical Properties	**Type 316L stainless steel**
Ultimate tensile strength, MPa	550
Yield strength, MPa	260
Elastic Modulus, GPa	193
Density,(g/cm^3)	7.9
Elongation,%	50

Table 2: Ideal biodegradable stent properties

	Ideal biodegradable stent properties
Mechanical properties	Ultimate tensile strength : 550 MPa Yield strength : 260 MPa Elastic Modulus : 193 GPa Density : 7.9 (g/cm^3) Elongation : 50% A sufficient radial force to avoid elastic recoil of the vessels Hydrodynamic compatibility [51]
Biological properties	Biocompatibility of the metal Non-toxicity of the degradation products
Chemical properties	Controlled degradation process
Surface properties	Adapted roughness
Lifespan	12-24 months
Others	Compatible with magnitic resonance imaging (MRI) and intravascular ultrasound (IVUS) [51] Radiopaque (addition of markers to make the stent visible by fluoroscopy is not required) [51]

The use of biodegradable polymer stents has been limited by some drawbacks such as local inflammation, radiolucency, limited mechanical performance and early recoil after implantation. In comparison, metal stents have great mechanical properties. Some of them even have properties strongly close to metal stents made of stainless steel, the gold standard material for stent applications [19]. Therefore, over the past two decades, biodegradable metal stents have drawn the attention of many scientists and researchers [53]. So far, two metallic biodegradable materials have been mostly investigated : magnesium-based and iron-based materials.

5.1 Mg-based alloys

5.1.1 Mechanical properties

Information on the mechanical properties and degradation rate of different magnesium-based alloys investigated for biodegradable stents can be found in Table 3. Since 316L stainless steel is the reference material, these properties are also presented as reference. In general, Mg and its alloys have mechanical properties that are relatively close to those of cortical bone (ρ = 1.99 g/cm^{-3} and E = 11.7–18.2 GPa). Therefore, they have a low density and too low rigidity (E = 41-45 GPa) for cardiovascular stent applications. In addition, their Young's modulus, also relatively low compared to 316L stainless steel, will be of benefit in reducing the stress shielding at the tissue-implant interface. As a result, Mg-based alloys seem to be more suitable for bone implants than for biodegradable cardiovascular stents, which require a higher Young's modulus [6].

Table 3: Mechanical properties of different magnesium-based materials investigated for biodegradable stents [6].

Material	**Yield Strength (MPa)**	**Tensile Strength (MPa)**	**Elongation (%)**
316L stainless steel	260	550	40
Pure Mg: as cast	20	86	13
WE43 alloy: extruded T5	195	280	2
AM60B-F: die cast	-	220	6-8
ZW21: extruded	200	270	17
WZ21: extruded	140	250	20

Recently, new Mg-based alloys have been developed in order to meet the requirements given in table 2. These newly developed biodegradable alloys, called ZW21 and WZ21, contain Zn, Y, Ca and Mn as alloying elements. They are manufactured using a technique based on microalloying, which gives them fine microstructural characteristics. Thanks to this, they exhibit high ductility and appropriate strength, which makes them suitable for stent applications [6, 18].

5.1.2 Corrosion mechanism

In an aqueous environment, magnesium generally degrades by reacting electrochemically with water to produce $Mg(OH)_2$ and H_2 [40]. The most common types of corrosion for magnesium and its alloys in a simulated physiological solution can be galvanic corrosion,

pitting corrosion, corrosion fatigue and erosion corrosion. *In vivo*, corrosion is much more complex than *in vitro*, because the degradation rate is affected by many factors such as presence of proteins, pH value changes, presence of amino acids, etc. [51]. However, *in vitro* corrosion tests are essential to estimate the degradation process that the material would undergo *in vivo* [49].

Body fluid is considered as an aggressive chloride environment in which magnesium degrades rapidly. For magnesium implants, it means that the fast degradation can overload surrounding tissues with the degradation products. This is one of the reason causing neointima formation and this is thus a risk factor for ISR. Too rapid degradation can also cause a loss of the mechanical properties integrity before the complete healing of the cardiovascular wall and therefore, it can highly limit the use of magnesium for cardiovascular biodegradable stents [6]. Alloying magnesium with elements such as aluminum, manganese and rare earth elements can be a solution to decrease its degradation rate [54]. For example, Mg-Y-Zn alloys are assumed to meet the degradation demands [18].

The overall corrosion reaction of all Mg-based alloys has not yet been completely studied. However, it is reasonable to assume that corrosion of pure Mg can also be applied to characterize the degradation of Mg-based alloys containing a high concentration of magnesium. Figure 7 illustrates a biocorrosion model for a Mg-Ca alloy in an aqueous solution. It allows to understand the corrosion processes at the alloy/aqueous solution interface. In this Mg-Ca alloy system, magnesium is still the component having the highest concentration. Therefore, to evaluate the degradation process of Mg-Ca alloys or other Mg-based alloys, the electrochemical mechanism of pure Mg can be used [40, 55] .

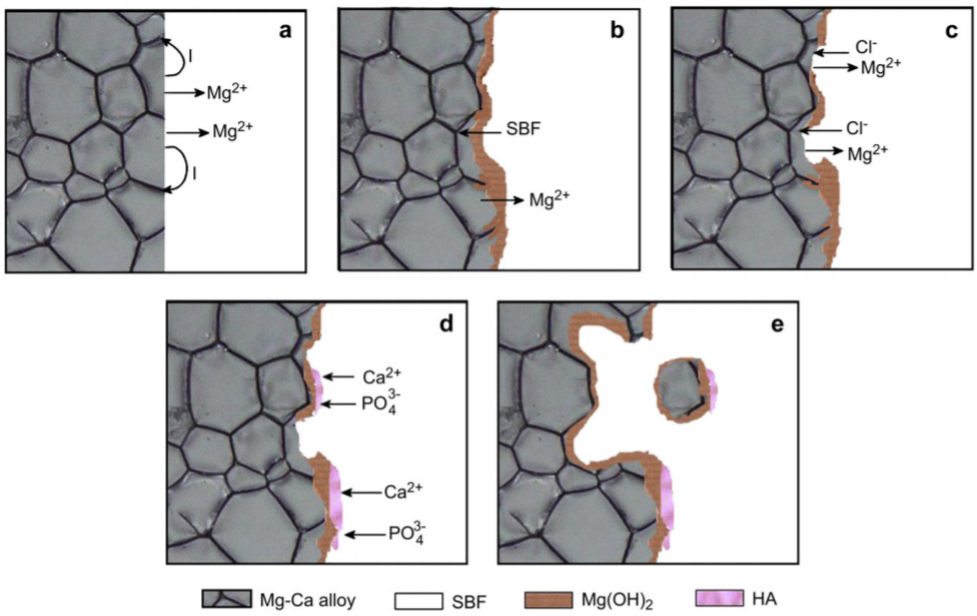

Figure 7: Schematic diagram of the Mg-based alloy/solution biocorrosion interface: (A) Galvanic corrosion between Mg and Mg_2-Ca phase. (B) Formation of a partially passive layer on the surface of the Mg-Ca alloy. (C) Adsorption of chloride ions at the interface and transformation of $Mg(OH)_2$ into $MgCl_2$ (D) Hydroxyapatite formation by the comsuption of Ca_2^+ and PO_4^{3-}. (E) Residues falling from the bulk substrate and degradation of the alloy [55].

5.1.3 Cytocompatibility

Mg is an important component and is present in large amounts in the human body. It is present in tissues to serve as a structural component. It is an intercellular cation which has an essential role in more than 300 cellular biological reactions. Magnesium is also considered to be a non-carcinogenic element [6]. An adult consumes up to 300-400 mg of magnesium per day. A very high consumption of magnesium is harmless to the human body and can be simply eliminated through the urine [51].

During corrosion of magnesium or Mg-based alloys, the anodic reaction (oxidation) is always coupled with a cathodic reaction associated with water decomposition. H_2 gas is also producted by a direct reduction of H^+ from H_2O. H_2 can be harmful if present in too large quantity. Its threat to biomedical applications depends on the spatial and temporal resolution of its production. If the production is slow enough, then H_2 gas can be tolerated by the human body. The same goes for the quantity. If the generated H_2 can be transported away from the production site so that its accumulation and build-up remains fairly low, there is no danger [56]. Stents are separated from the bloodstream by a small diffusion barrier made up of neointima. Therefore, H_2 gas can easily join the bloodstream and no build-up is expected to occur near the stent. [57].

Surface alkalization can also occur due to Mg dissolution. This is an aditionnal concern that can limit the use of Mg-based alloys for biomedical applications. Indeed, in non-buffered solutions, Mg dissolution can lead to high values of pH (pH 10–12). Even in buffered solutions, the degradation of Mg-based alloys is always coupled with an increase in pH [56]. A very high increase in pH can have dramatic consequences on the functioning of cells and their performance by decreasing their viability and metabolic activity. However, permanent blood fluid exchange makes it possible to avoid a build-up of the degradation products where they originate. Therefore, it is reasonnable to assume that the increase in pH observed during *in vitro* experiments will be much smaller *in vivo* [18].

5.2 Fe-based alloys

5.2.1 Mechanical properties

Iron is an interesting candidate for biodegradable stents in terms of its mechanical properties [6]. Indeed, mechanical properties of iron are comparable with those associated with metals for permanent cardiovascular implants. Iron has a high radial strength because of its high elastic modulus (E = 162-170 GPa). This can be helpful when making stents with thinner struts. Iron has also a high ductility which can be helpful during the implantation of the stent when it is plastically deformed [6]. Moreover, Peuster *et al.* have shown that iron stents can maintain their mechanical properties during an implantation from 6 to 18 months without any failure. As part of this study, stents were implanted in the descending aorta of New Zealand white rabbits [58].

Table 4 presents the data of mechanical properties of different iron-based materials for biodegradable stents. They are compared to the mechanical properties of Armco® iron which has already been tested during *in vivo* experiments. The properties of 316L stainless steel are also presented as reference.

Table 4: Mechanical properties of different iron-based materials investigated for biodegradable stents [6]

Material	**Yield Strength (MPa)**	**Tensile Strength (MPa)**	**Elongation (%)**
316L stainless steel	260	550	40
Armco® Fe: annealed	150	200	40
Fe-35Mn alloy: annealed	230	430	30
Fe-10Mn-1Pd alloy: heat treated	850-950	1450-1550	2-8
Electroformed Fe: annealed at 550 °C	270	290	18
Fe alloyed by different elements (Mn, Co, Al, W, Sn, B, C and S): as cast	100-220	190-360	12-23
Fe-30Mn-6Si alloy: solution treated	180	450	16
Nanocrystalline Fe: ECAP, 8 passes	-	250-450	-

.

5.2.2 Cytocompatibility

Iron is an essential trace element found in nearly all living organisms. It constitutes an essential chemical compound for many enzymes which are involved in various physiological processes such as oxygen binding, DNA synthesis and redox enzyme activity. Uptake and intracellular iron accretion are highly regulated processes that are controlled by complex mechanisms at different levels. However, a too high quantity of iron can be dangerous. When an iron implant corrodes, the degradation products can overload and affect surrounding tissues. [51]. Among others, Peuster *et al.*, who have implanted iron stents in descending aorta of New Zealand white rabbits, have analyzed the cytocompatibility. No significant evidence of an inflammatory response or neointimal proliferation has been revealed after analysis of the results and organs examination did not demonstrate any systemic toxicity [58]. An other study, still conducted by Peuster *et al.* a few years later, where stents were implanted into the descending aorta of 29 mini-pigs, led to the same conclusions. Indeed, despite the death of two animals after the stent implantation, the histopathological analysis of the heart, lung, spleen, liver, kidney and para-aortic lymphatic nodes of the remaining 27 mini-pigs showed no signs of iron overload or iron-related organ toxicity [59].

Those studies are based on pure iron biodegradable stents. Generally, in the case of Fe-based alloys, the release rate of iron ions and alloy components is not proportional to their composition in the alloy. The analysis of related-iron effects on the cytocompatibility should be done by taking into consideration this non proportional relationship. Moreover, the effect of ions as single elements may be different from that of these ions in the mixture; additive or synergistic effects may exist. [60].

However, many *in vitro* cytotcompatibility studies performed on iron and on Fe-based materials have been published and have demonstrated no or very low toxicity to different types of cells. Additionally, several *in vivo* tests with Fe-based alloys have revealed no adverse effect on surrounding tissues, organs or the nervous system. Based on those investigations and studies, iron can be considered as a promising candidate to produce biodegradable implants [53].

5.2.3 Corrosion mechanism

In aqueous environment, the corrosion of Fe-based alloys is not coupled with hydrogen evolution like Mg and Mg-based alloys. The degradation mechanism of Fe in Hank's solution, a common simulated physiological solution, can be described as follows. When the surface of Fe is exposed to the solution or is in contact with the solution flow, it is oxidized and Fe^{2+} is formed. Under the condition of alkaline pH and the oxygen environment of the simulated physiological fluid, some of the Fe^{2+} ions are further oxydized to form Fe^{3+} and $Fe(OH)_3$ is then produced. It is followed by the hydrolysis of $Fe(OH)_3$ and the precipitation of goethite (α-FeO(OH)) due to the presence of chloride ions and an aerated solution. Magnetite is then formed by the reaction of $Fe(OH)_2$ with FeO(OH). The precipitation of calcium and phosphor elements from the solution, and the formation of hydroxide and oxide at the surface of Fe, are the main reasons for the inhibition of further corrosion [40].

Therefore, the *in vivo* degradation rate of a pure iron stent is too low. Hermawan *et al.* have calculated the degradation rate of pure Mg and pure Fe using three degradation *in vitro* tests. Results (in millimeter per year (mmpy)) can be found in Table 5 and clearly show that pure Fe has a much slower degradation rate than Mg. In the static immersion test, the effect of exposure time can be observed. The corrosion rate varies between 48 hours and 168 hours of exposure time. The decrease in corrosion rate of pure Fe is due to the formation of a protective layer containing calcium and phosphor that prevents further corrosion [61].

Table 5: Corrosion rate for pure Mg and pure Fe obtained from potentiodynamic polarization and static immersion tests. [a]after 48 hours; [b]after 168 hours

	Corrosion rate (mmpy)		
	Potentiodynamic polarization	Static immersion	
pure Mg	407,90	205.53[a]	N/A
pure Fe	0,19	0.20[a]	0.23[b]

A lot of research is currently being carried out in this field with the aim to increase the corrosion rate of pure Fe by modifying the alloy composition and the microstructure of the metal [6]. Many articles suggest that an effective solution for increasing the degradation rate is to implement more noble or conductive inert phases in the metal. These phases then act as cathode phases, and the corrosion of the less noble matrix is improved [6, 19, 53, 62]. Another approach is to modify the microstructure of the metal by selecting an appropriate processing technique, by choosing a suitable alloying or by modifying the heat treatment parameters correctly [19].

An *in vitro* corrosion mechanism for Fe-X binary alloys in simulated physiological solution can be described as follows. Figure 8 shows the corresponding schematic illustration [63].

1. Initiation : When a binary Fe-X alloy is immersed in a simulated physiological solution, anodic dissolution of iron occurs and iron(II) hydroxide is formed by the combination of OH ions and Fe^{2+}. Fe^{2+} can be further oxidized due to the presence of dissolved oxygen in the solution.

2. Formation and growth : Passive layer breakdown can occur because of the accumulation of chloride ions at the surface of the metal in contact with the solution. After passive layer breakdown, a corrosion product layer will cover any pits formed by the corrosion. There can be significant changes inside the pits because of localized acidification and accumulation of chloride ions. Due to the formation of a layer composed of Ca and P elements precipitated from the solution on the surface of the alloy, the corrosion of iron is self-catalytic. Therefore, the corrosion potential is reduced as the corrosion progresses.

3. Development after 6 months : After being immersed for 6 months in the simulated physiological solution, the binary Fe-X alloys ended up in two different situations. In the first one, the pit became increasingly larger and deeper, while corrosion on the rest of the surface of the alloy remained inhibited by the presence of the passive layer. In the second situation, a thick layer composed of corrosion products had covered the entire surface of the alloy. This layer of corrosion products made it possible to reduce the impedance, and the anodic dissolution of the iron was therefore improved.

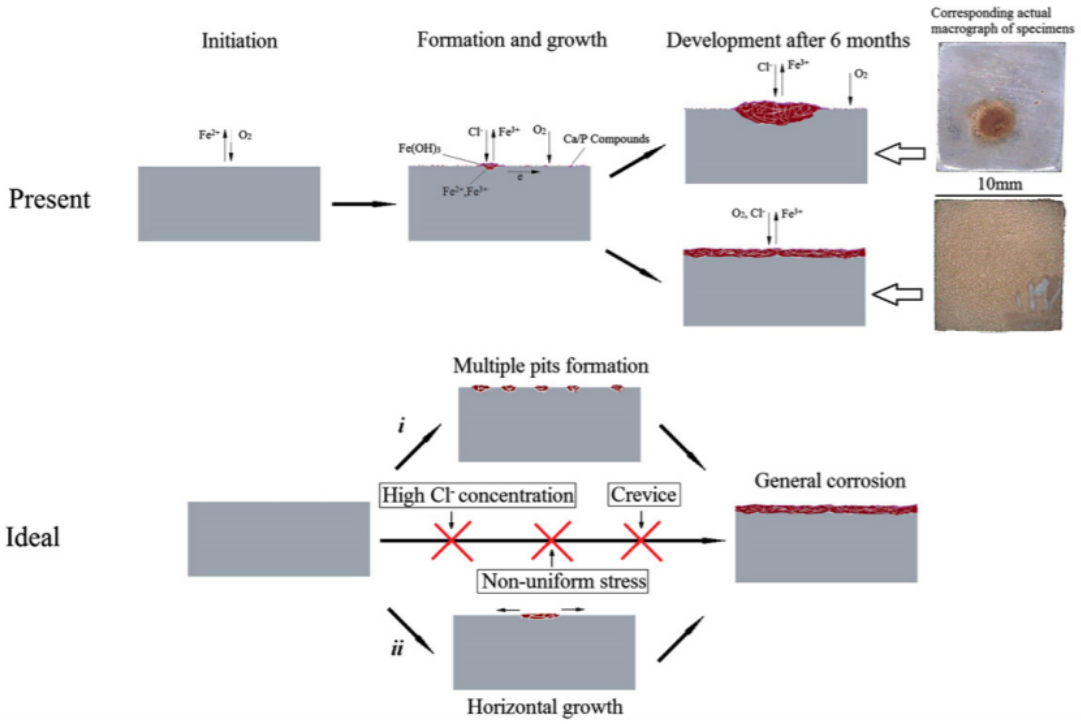

Figure 8: Schematic diagrams illustrating both the corrosion mechanism and ideal corrosion process of Fe-based biodegradable alloys in Hank's solution [63].

In theory, localized corrosion is undesirable for potential candidates for biodegradable cardiovascular stents because it can be a source of local failure. The degradation rate also becomes uncertain. A solution with a high concentration of chloride ions as well as crevices are risk factors for localized corrosion. Unfortunately, the blood plasma contains a high concentration of chloride ions and crevices can form between the deployed stent and the arterial wall. Localized corrosion can also be caused by a non-uniform distribution of

stresses along the stent after the deployment of the latter.

To improve the corrosion of binary Fe-based alloys in the blood environment, two different strategies are possible, as shown in the ideal corrosion process in Figure 8. (i) Mutliple pits should form on the surface of the metal during the formation and growth stages. The pits will then enlarge and widden until they join and become connected to form a continuous layer of corrosion products on the surface. This type of corrosion is possible if all the metals present beneath are in the same corrosion product coverage condition. This ideal corrosion mechanism can be realized by decreasing the pitting potential or by introducing a widespread secondary phase intermetallic network. (ii) A unique pit should form and it should grow in the horizontal direction. In theory, this is very complicated because of the self-catalytic behaviour of iron corrosion. To address this issue, the corrosion potential can be increased or localized acidification can be inhibited [63].

Therefore, adequate alloying should be done to enhance the corrosion rate and mechanism. Both the concentration and the number of alloying elements should be selected carefully in order to obtain a higher corrosion rate and a uniform degradation [63]. For example, Liu *et al.* have proven that the corrosion rate of pure iron decreased when 3 at.% Mn is added [63]. Whereas according to Hermawan *et al.*, the corrosion rate was found to be twice as fast as pure iron when 35 at.% Mn is added [61]. Also, according to Schinhammer *et al.*, the addition of Pd to an Fe-Mn alloy (Fe–10Mn–1Pd (in wt.%)) was reported to effectively improve the corrosion rate [64].

5.2.4 TWIP alloy

As explained above, the *in vivo* degradation rate of pure iron is too low. Recently, a lot of research has been focused on increasing the corrosion rate of iron-based materials by changing the alloy composition, modifying the material structure design or introducing corrosion-promoting substances or mechanisms.

At UCLouvain, TWIP has been developed in order to meet the specifications listed in Table 2 and therefore to increase the corrosion rate while maintaining adapted mechanical properties of pure iron and a good cytocompatibility. The TWIP alloy is the material of focus of this thesis and is composed of Fe-Mn-Si-Al. TWIP alloys exhibit twinning induced plasticity, which gives them very good ductility and strength as a result of their high strain-hardening capacities. The TWIP wires used in this thesis are manufactered by Professor Pascal Jacques and their composition can be found in Table 6.

Table 6: TWIP composition

	%wt content						
	Al	Cr	Cu	Fe	Mn	Ni	Si
TWIP	0,92	0,03	0,02	74,8	23,1	0,03	1,02

5.3 Characterization techniques for stents

As for ISR, histology, computer simulations or microCT and CE-CT techniques can be used to characterize the state of a stent after its implantation (i.e. *in vivo*) or *in vitro*. Vorpahl *et al.* have combined microCT and histology to characterize the natural history

of stented arteries. First, microCT imaging was performed followed by an histological analysis to answer remaining pathoanatomical questions after the microCT analysis. During microCT, the specimens are kept intact. This allows for subsequent histological analysis. MicroCT imaging of stented arteries can provide insight into stent-stent interactions (treatment of bifurcations or long lesions can demand multiple and/or overlapping stents), calcified lesions or the vessel wall. It also provides valuable information regarding the relationship between stent implantation and stent thrombosis, and enables a detailed analysis of the various types of stent fracture. This tool provides a significant complement to histopathological analysis of ex vivo stented arterial segments and allows for a more complete understanding of the natural history of the stented arterial segment. However, imaging can only be done ex vivo since microCT can not be used for *in vivo* human imaging [24].

In the framework of this master thesis, MicroCT will be optimized for its use to characterize the state of the stent *in vitro* and, more particularly, its roughness and its corrosion rate after *in vitro* degradation. It is hypothesized that these data will allow us to better predict the structural transformations that the stent would undergo *in vivo* and therefore correlate them with a possible risk of ISR.

6 *In vitro* degradation

Before performing *in vivo* studies, *in vitro* tests need to be carried out to investigate the degradation behaviour of a biodegradable material, which could potentially be used for stents. Therefore, *in vitro* test methods can be used to select the materials that are best suited for further *in vivo* studies. Early signs of cell compatibility of the alloys also need to be assessed but since this master thesis focuses on corrosion rate and roughness analysis, only methods used to characterize the *in vitro* degradation of stents will be detailed in what follows [48]. Standards are available to guide scientists to perform degradation tests. In particular, the ASTM F2129 [65] and ASTM G59 [66] can be useful since they describe methods for preparing test specimens and conducting potentiodynamic polarization tests. The ASTM G31 [67] is well suited for laboratory immersion corrosion tests [61].

6.1 Simulated physiological solution

To try to better understand the *in vivo* corrosion data via *in vitro* tests, one of the most essential factors is to use a suitable simulated physiological solution. Various solution systems have been used to mimic the body fluid. The main solutions include: 0.9% NaCl aqueous solution, simulated body fluid (SBF), Hank's solution, phosphate buffered saline (PBS), Dulbecco/Vogt modified Eagle's minimal essential medium (DMEM)... The detailed inorganic compositions of several common simulated physiological solutions are compared to human blood plasma inorganic composition in Table 7.

Materials show different degradation behaviors in different solutions. Both inorganic ions and organic components have an important influence on the corrosion process of metal alloys, so composition of the solution must be chosen cautiously. A buffer electrolyte solution containing similar components than human blood plasma should be used to conduct *in vitro* degradation tests [40].

Table 7: Inorganic composition of common simulated physiological solutions compared with human blood plasma.

Chemical composition	Human blood plasma	SBF	Hank's solution	DMEM	PBS
Na^+	142	142	141,6	155,3	137
K^+	5	5	5,4	5,3	2,7
Mg^{2+}	1,5	1,6-2,5	1,3-2,5	1,8	-
Ca^{2+}	2,5	1-1,5	0,75-0,87	0,8	-
Cl^-	103	103-148,8	144-147	115,7	-
HCO_3^-	27	4,2-27	4,2	44,1	-
HPO_4^-	1	1	0,3	0,9	10
SO_4^{2-}	0,5	0,5	0,26-0,8	0,8	-

6.2 Immersion tests

Immersion tests are common methods to assess the corrosion properties of biodegradable metallic materials. Tested materials are corroded in a testing solution. The corrosion products can be analyzed by a series of methods. The test cell should be tightly closed to avoid evaporation and, be maintained at 37°C for the desired duration.

Tests are divided into static and dynamic immersion tests. In static immersion tests, the samples are immersed in a static solution, whereas in dynamic immersion tests, the samples are exposed to the solution flow. Most reports use static immersion tests to evaluate the corrosion properties and behavior of metallic materials. However, some results reveal that data of these type of *in vitro* corrosion are not able to predict *in vivo* corrosion. Therefore, a series of dynamic immersion tests have been created to better simulate the *in vivo* environment [40]. According to Hermawan *et al.*, the conditions in human coronary arteries (where blood with viscosity of 3,0–4,0 mPa*s and density of 1,06 g/cm^3 flows at the average speed of 7,2–25 cm/s and introduces wall shear stress of 0,33–1,24 Pa) were almost successfully met with the test-bench shown in Figure 9 and created by Levesque *et al.* [61, 68]. The simulated physiological solution was flowing in a closed-loop system creating a laminar flow inside the test chamber sweeping the samples surface [61].

In this master thesis, a dynamic immersion test will be used to analyse the *in vitro* degradation.

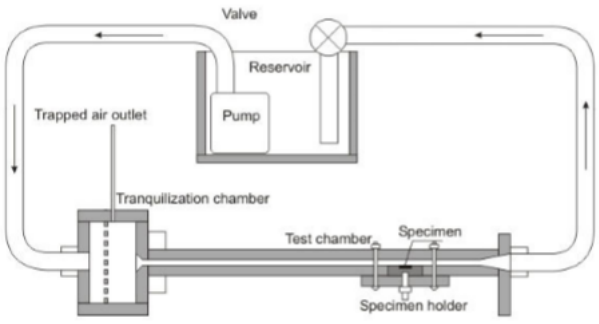

Figure 9: Dynamic immersion test [61]

6.3 Electrochemical tests

Electrochemical tests are convenient, easy and fast methods to evaluate the corrosion properties of a metal by testing the open circuit potential (OCP), the polarization curves or the electrochemical impedance spectroscopy (EIS) via a three-electrode system [40]. A potentiostatic circuit (Figure 10) is composed of [69] :

- a polarization cell,
- a working electrode (WE), which is the corrosion sample (i.e., the material under evaluation),
- a counter electrode (CE), which is ideally made of a material that will support electrochemical oxidation or reduction reactions with reactants in the electrolyte, but will not be correded and contaminate the electrolyte solution with its degradation products,
- a reference electrode (RE), which maintains a constant potential. The potential of the WE is measured relative to this potential with an electrometer.
- a potentiostat, which maintains the difference between the potential of the WE and the potential of the RE constant, even though the external circuit current, i_{ex}, may change by several orders of magnitude.

When the potentiostat is disconnected from the corrosion sample (WE), the open-circuit condition is met, the WE is freely corroding and the OCP can be measured. A computer can display a polarization curve where the current density is plotted against the electrode potential. Polarization curves are valuable in quantifying the behaviors of metals under various conditions. EIS is introduced as an alternating current (AC) technique. It has been used in corrosion research to estimate the corrosion rates and to study the passivation of metals [70]. In this study, however, we did not have the availability of this type of measurement.

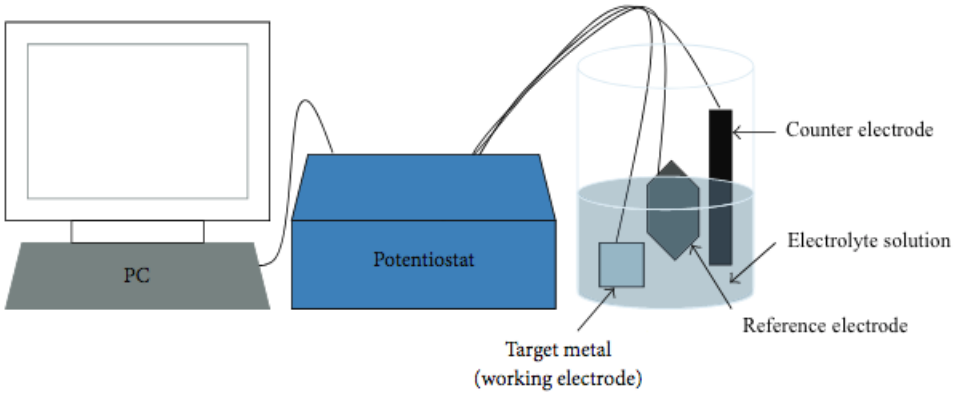

Figure 10: Electrochemical test. Adapted from [71].

6.4 Evaluation of the corrosion rate

6.4.1 Mass loss

Mass loss is a method for assessing the corrosion rate by measuring the mass change of samples before and after immersion. The sample is soaked in the electrolyte solution

for a period of time. The sample is then removed and the change in mass is evaluated. The corrosion rate can be calculated based on the mass loss of samples according to the following equation [19, 61] :

$$CR = 8,76 * 10^4 * \frac{W}{A * t * \rho} \tag{1}$$

Where CR (corrosion rate) is in mm per year (mmpy), W is the mass loss (g), A is the area of the sample exposed to the electrolyte solution (cm^2), t is the time of exposure (h) and ρ is the material density (g/cm3).

6.4.2 Hydrogen evolution

Hydrogen evolution can only evaluate the corrosion rate of metals which can produce gas when immersed in simulated physiological solutions, such as Mg-based alloys. The principle is based on the corrosion reaction of magnesium. The dissolution of 1 mol of Mg generates 1 mol of H_2. From the ideal gas law and the volume of H_2, the mass loss of Mg can be calculated (1 mL of H_2 = 0.001083 g of Mg) and subsituted in Equation 1. Therefore, the measurement of H_2 is equivalent to the measurement of mass loss of Mg. Different from the mass loss method, hydrogen evolution evaluation is a real-time dynamic observation of the corrosion process. So, the change trend of corrosion rate can easily be tracked by measuring the hydrogene concentration multiple times during the experiment [40, 72].

6.4.3 Electrochemical corrosion current

Other methods to determine the corrosion rate *in vitro* are gravimetric and electrochemical measurements. The corrosion rate can be calculated by using the following equation [61] :

$$CR = 3,27 * 10^3 * i_{corr} * \frac{EW}{\rho} \tag{2}$$

Where CR is in mm per year (mmpy), ρ is the density (g/cm^3), i_{corr} is the corrosion current density ($\mu A/cm^2$) and EW is the equivalent weight (g/eq).

6.4.4 Released ion concentration

The released ion concentration in the immersion solution is another way to evaluate the corrosion rate of metals. The immersion solution is digested by adding acid, and inductively coupled plasma-atomic emission spectrometer (ICP-MS) is used to calculate the ions concentration in the solution. The equation to compute the corrosion rate is then given as follows [40]:

$$CR = \frac{cV}{St} \tag{3}$$

Where CR is in $g/(m^2 \cdot day)$, c is the ion release concentration (g/mL), V is the volume of the immersion solution (mL), S is the original surface area exposed to corrosive media (m^2), and t is the exposure time (days).

To evaluate the degradation in this master thesis, both the released ion concentration and the mass loss methods were used. All of the methods described above are indirect method. MicroCT could provide a direct measure of the degradation rate as well as insight into

the change in roughness over time, two parameters that have been investigated in this master thesis.

Part III
Problem statement, aims and objectives

Fe-based alloys seem to be promising candidates for intravascular biodegradable stent applications. They enable appropriate values of mechanical properties and many *in vitro* and *in vivo* citotoxicity studies have shown no or very limited toxicity to different types of cells and no adverse effect on adjacent tissues, organs or the nervous system. However, a controlled degradation process seems to be difficult to obtain. Yet, a controlled degradation rate is essential during the arterial vessel remodelling process to allow for a complete healing of the latter. Also, the roughness is known to have an important influence on the stent performance. A smooth surface could reduce thrombogenicity and neointimal proliferation while a rough surface could accelerate stent endothelialization and increase the capacity of anti-restenotic drug storage. However, surface analysis is rarely analysed in the literature and effects of roughness are sometimes neglected. Moreover, for the analysis of the degradation rate and roughness, a detailed characterization of the stent is required. This is what is driving the research done in this master thesis.

Studying *in vitro* degradation and roughness of candidate materials for biodegradable stent application and gathering a 3D reconstruction of the samples before and after immersion thanks to microCT is something that has not been done yet. Generating a 3D set of images with microCT is, therefore, a new way of studying degradation rate and roughness. It is also useful to screen and select candidate materials for intravascular biodegradable stent technology. Therefore, one of the main objectives of this work is to assess and optimize microCT for the characterization of the degradation rate and the roughness evolution over time. For this purpose, the roughness and degradation rate of wires made of TWIP and pure iron will be analysed during *in vitro* dynamic immersion tests.

This work will be divided in two main parts. Firstly, the degradation rate will be analysed using microCT and will be compared to mass loss measurements. It will also be evaluated based on the *in vitro* released degradation products, again in combination with the mass loss method. Secondly, roughness of the wires at different immersion times will be analysed. In order to set-up a robust characterization protocol for roughness measurements of stents, this will be done using different microCT-based methods, and then methods will be compared.

Off note : due to the strict Coronavirus measures, the objectives of this master thesis have been modified compared to those initially planned. I was on Erasmus in the first half of the year. I was supposed to follow the safety seminar in the second semester to get access to the laboratories and was planning to start my experimental work during the week of the 16th of March. But due to the lockdown, I was no longer allowed to work in the lab, and, in agreement with my promoter and daily contact, it was decided to cancel all the experimental work. It would have focussed on ICP-MS and comparing the *in vitro* and *in vivo* behaviors of both materials using microCT. I had also planned to study the interaction between stent and tissue.

Part IV
In vitro degradation

1 Materials and methods

The experiment described in this section have been conducted by Léa Paulus in her thesis (2018-2019) and by my daily supervisor, PhD student Lisa Leyssens. Information on the procedure has been collected from Léa's thesis [73]. I only processed the gathered data, which was not performed previously. The main procedure steps can be found in Table 8. Each step are then detailed in the rest of this section.

Table 8: Main procedure steps of the experiment.

	Steps
1	Wires production
2	Scanning of all wires with microCT
3	Immersion tests
4	Scanning of all wires using microCT after immersion
5	Measurement of the degradation rate and surface roughness by comparing scans before ad after immersion
6	Measurement of the degradation rate through ICP-MS results and comparison with degradation rate results found using microCT scans

1.1 Sample production

The production of tubular stents is expensive. This is the reason why wires instead of tubes have been used. Compared to tubes, wires are relatively easy and cheap to produce. Due to the similarities of the drawing process, both wires and tubes made of the same material presumably show reasonably comparable properties [74]. The wires have been made of TWIP (Fe-Mn-Al-Si) and pure iron. Dimensions of the wires are given in Figure 11.

(a) Cylindral pure iron wire dimensions. (b) Rectangular TWIP wire dimensions.

Figure 11: Samples dimensions.

1.2 Sample preparation

Before immersion, pure iron and TWIP wires were weighted using a balance with a μg precision. Then, wires were cleaned with oxygenated water and washed with ethyl alcohol.

Finally, they were dried with an absorbing tissue.

1.3 Immersion test

The immersion test set-up can be seen on Figure 12. Before filling the falcon tubes with SBF, the temperature and the pH of the electrolyte solution were measured. Then, 15 mL of a solution composed of SBF and HEPES (a common buffer for SBF) was poured into the falcon tubes and one wire of TWIP or pure iron was added to each tube. One sample tube was kept empty to serve as a control sample. Samples were then harvested at different immersion times.

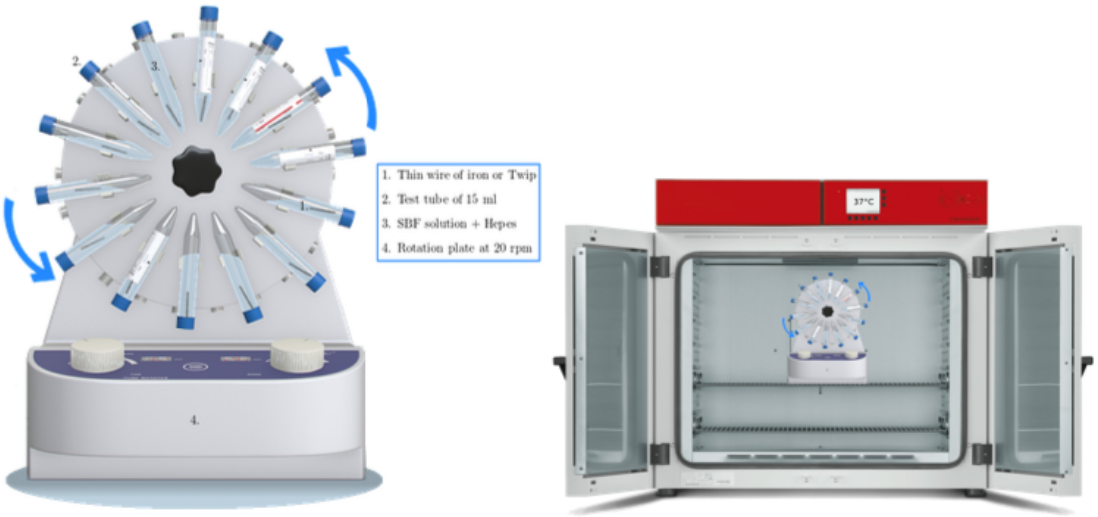

Figure 12: Dynamic immersion test [73].

Simultaneously, the test tubes were placed on a rotating plate, which was inserted in a preheated stove at 37°C . During the dynamic immersion test, a rotational speed of 20 rpm and an oven temperature of 37°C were maintained. This up and down movement of the wires, induced by the dynamic immersion test, was chosen to virtually mimic the blood flow and conditions in human arteries.

The different time points have been determined with a particular attention. It was important to have a good overview of the entire degradation process. Indeed, ideally, degradation should begin at a very slow rate to keep optimal mechanical integrity of the stent during the arterial vessel remodelling process. Then, as the mechanical integrity decreases, the degradation should progress at a sufficient rate without causing an intolerable accumulation of degradation products around the implantation site. This is why, an early time point after 5 hours of immersion and a late time point after 7 days of immersion were chosen. To characterize the evolution of the degradation rate, a third time point was set after 24 hours of immersion. These time points were also chosen in accordance with the literature.

After each time point, test tubes were removed from the rotating plate. Then, the solution was decanted and its pH was measured. Samples were then washed following the same

procedure described above.

Samples were scanned using microCT prior to and after the immersion. Therefore, particular attention was needed to remember the direction of the wire to ensure that both scans would be done properly.

1.4 *In vitro* degradation products analysis

The *in vitro* degradation products in the electrolyte solution were analysed to evaluate the degradation rate with ICP-MS. This type of mass spectrometry uses an inductively coupled plasma (ICP) to ionize the sample. It atomizes the sample and creates atomic and small polyatomic ions, which are then detected. It is known and used for its ability to detect metals and several non-metals in liquid samples at very low concentration rates. Those are then used to calculate the mass loss (Equation 1) considering the composition of the sample.

For the ICP-MS results, iron ions were used to evaluate the degradation rate for pure iron wire samples. For TWIP samples, only iron and manganese ions concentrations were used since no concentrations of aluminium and silicon ions were detected in the solution.

1.5 MicroCT

MicroCT datasets were gathered from the three different time points for pure iron. For the TWIP samples, due to time and technical limitations, only five samples were produced. Therefore, only data after 5 hours of immersion was obtained.

The MicroCT scanning was done using the Phoenix nanotom M. The optimal resolution is based on a tradeoff between field of view, spatial resolution and file size. For example, to acquire an image of a specimen with a large region of interest (long wire), the specimen must be positioned further away from the X-ray source, which results in a lower magnification and spatial resolution. Alternatively, smaller regions of interest (ROI) can be scanned by positioning the sample closer to the X-ray source and this, in turn, results in increased magnification and higher resolution [24]. Hence, in order to increase the resolution of the scans, necessary for the roughness measurements, it was assumed that the degradation rate was homogeneous and therefore, the samples were only scanned on a length of 2394 μm and at a resolution of 1 μm. The homogeneity of the degradation rate and also the roughness has been assessed by using different analysis methods, which evaluate the degradation rate on different lengths and by doing roughness measurements on smaller and larger ROIs. To scan the same part of the sample prior to and after the immersion, scans were made in the middle of the wires.

1.5.1 Degradation rate

For image processing and analysis, the software CTAn was used [75]. After importing the microCT reconstructed images of each sample in the software, an automatic threshold (Otsu method) was applied to obtain a binary image and a 3D morphological analysis was performed for each sample.

Volumes before and after immersion were computed on two different set of images. First, they were calculated on the complete dataset and therefore on 2394 images. Second, they were assessed using only 1000 images located at the center of the sample. Then, the mass loss (Equation 1) was calculated and the degradation rate of each sample was determined either after 5 hours, 24 hours or 7 days of immersion.

1.5.2 Roughness

The roughness of each sample was computed using the microCT-based surface roughness measurement protocol from Kerckhofs *et al.* [39]. After successfully acquiring a scan, the dataset is reconstructed. The reconstructed images can be loaded in DataViewer (Bruker) to view a 3D representation of the sample as well as each 2D cross-section in the sagittal, coronal and tranverse planes [75]. The roughness parameters can then be computed using the profile lines of the binarized 2D cross-sectional microCT images (Figure 13). These profile lines were extracted using a developed Matlab routine. The following surface roughness parameters were estimated in correspondence with ISO 4287-1997 [76] :

– The arithmetic mean absolute deviation of the roughness profile :

$$R_a = \frac{1}{n}\sum_{i=1}^{n}|y_i| \tag{4}$$

– The root mean square deviation of the roughness profile from the mean line :

$$R_q = \sqrt{\frac{1}{n}\sum_{i=1}^{n}y_i^2} \tag{5}$$

– The total height of the roughness profile :

$$R_t = R_p - R_v \tag{6}$$

Where n is the number of data points in the X-direction, y is the surface height relative to the mean plane, R_p is the maximum profile peak height and R_v is the maximum profile valley depth.

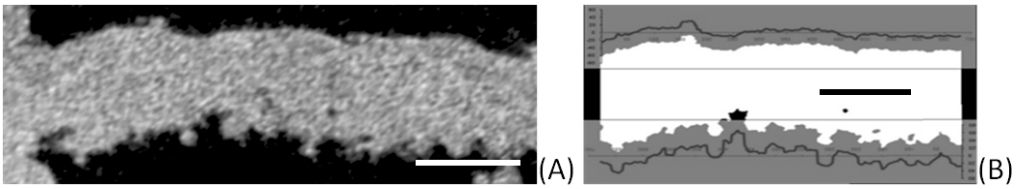

Figure 13: MicroCT-based surface roughness measurement with the profile lines of 2D cross-sectional microCT images. (A) A typical high resolution (voxel size = 1.5 μm) 2D microCT cross-sectional image. (B) A binarized image of (A) with the corresponding profile lines. Scale bars = 200 μm [39].

In total, 8 images were collected per wire, thus, allowing for 16 measurements of the roughness since the latter was evaluated on both sides of the image. Indeed, two profile lines (red lines) were extracted from each 2D cross sectional image (Figure 14a).

For the moment, there is no tool able to calculate the roughness in 3D. However, the roughness is heterogeneous so a 3D analysis is needed and only one 2D measurement is not enough. Due to this limitation, it was expected that choosing 16 profile lines all around the sample could allow us to have a good overview of the roughness in 3D. To analyse the homogeneity of the roughness around the samples, and the influence of the number of profiles lines, analysis of the roughness was also done with 8 profile lines. (Figure 14b)

(a) Roughness evaluation using 16 profile lines (b) Roughness evaluation using 8 profile lines

Figure 14: Profile lines for a cylindrical sample.

Depending on the arithmetic mean absolute deviation of the roughness profile, evaluation lengths required for correct analysis can be found in Table 9, from the ISO4288:1996 [77]. If R_a is superior to 0,1 μm, which was the expectation, the roughness evaluation length (l_n) should be 4 mm. However, for the samples investigated, the average profile length available for measurement was only about 2,394 mm. Therefore, the long measurements were made along the entire length of the wire. Short measurements were also made on the upper third of the wire and therefore on a length of 0,798 mm to analyse the homogeneity of the roughness and the influence of the waviness. Indeed, the waviness of the roughness profile is not taken into account with the evaluation length. The roughness sampling length (l_r) is defined as the cut-off length (λ_c) of the filter used to separate roughness from waviness. Therefore, it corresponds to the distance required in order to include small enough irregularities for a relevant roughness evaluation, excluding non-relevant long wavelength components. Usually, five measurements of length l_r are made along the evaluation length [76].

Table 9: Roughness sampling lengths for the measurement of R_a

R_a (μm)	**Roughness sampling length, *lr* (mm)**	**Roughness evaluation length, *ln* (mm)**	**Cut-off, λ_c (mm)**
(0,006) $<R_a \leq 0,02$	0,08	0,4	0,08
0,02 $<R_a \leq 0,1$	0,25	1,25	0,25
0,1 $<R_a \leq 2$	0,8	4	0,8
2 $<R_a \leq 10$	2,5	12,5	2,5
10 $<R_a \leq 80$	8	40	8

The roughness was measured using two different Matlab routines. The first Matlab routine (named code 1 in the rest of the text) is a 2D analyser, which can only deal with straight surfaces (waviness of the surface is not taken into account). One linear baseline is displayed (green line) and is supposed to follow the profile line of the 2D cross-sectional image (red line). Therefore, it is not possible for the baseline to follow the curvature of the wire. The roughness is then evaluated by computing the distance between the green line and the red line (Figure 15a). If the wire is not completely straight, a big error can happen. That is why a second Matlab routine was used (named code 2 in the rest the text). Points along the wire can be chosen (Figure 15b). A linear baseline is then created between each point and again, the distance between the red line and each baseline is computed. Eight different points along the surface were used. Therefore, according to ISO standards, waviness should be taken into account since each measurement is made on a distance eight times smaller than the initial evaluation length l_n. However, waviness of a sample may vary and a linear baseline will never be completely able to take it into account. To overcome this limitation, a third Matlab routine, allowing for the replacement of the linear baseline between each point by a polygonal baselines, is also available. With this tool, the waviness can fully be taken into account. Unfortunately, due to the lockdown, the tool was not accessible.

(a) 2D roughness computation using a single linear baseline (code 1).

(b) 2D roughness computation using multiple linear baselines (code 2).

Figure 15: 2D roughness computation.

To conclude, the following topics will be covered and analysed : the influence of the number of profile lines, the homogeneity of the roughness, the comparison between both Matlab routines and their limitations, the variation of the roughness over time, the comparison of the roughness of TWIP with pure Fe and the influence of the initial roughness on the degradation rate. Reasons that motivate the choice of these topics can be found in Table 10.

Table 10: Topics covered and analysed in this master thesis as well as the motivations behind them.

Topics	Motivations
Influence of the number of profile lines (16 versus 8)	- Analysis of the homogeneity of the roughness around the sample. - Detection and consideration of outliers.
Homogeneity of the roughness (smaller versus larger ROIs)	- Analysis of the homogeneity of the roughness along the sample. - Analysis of the influence of the waviness and the incapacity of code 1 to take it into account.
Comparison between both Matlab routines and their limitations	- Selection of the best Matlab routine for roughness analysis.
Variation of the roughness over time	- Evolution of the roughness over time knowing that the latter has a significant influence on ISR. - Selection of the best candidate materials for biodegradable stent applications.
Comparison of the roughness of TWIP with pure Fe	- Influence of the manufacturing process on the roughness. -Difference in the evolution of the roughness between both materials. - Selection of the best candidate materials for biodegradable stent applications.
Influence of the initial roughness on the degradation rate	- Verification that the degradation has correctly been increased by alloying and not by the initial roughness.

1.6 Statistical analysis

A statistical analysis was then performed on the data. First, outliers were removed using the Dixon test available on the AnaStats website [78]. Then the normality test of Shapiro & Wilk, also available on the AnaStats website, was done [79]. Finally, to compare the average roughness parameters between :

- 16 and 8 profiles lines,
- small and large ROIs,
- code 1 and code 2,
- the different time points,
- pure Fe and TWIP,

Student t-tests were conducted using GraphPad [80]. For all results, p-values were determined and considered not significant if larger than 0,05.

2 Results and discussion

2.1 Degradation rate

2.1.1 ICP-MS

After the *in vitro* degradation test, the electrolyte solution of each tube was collected and analysed using the ICP-MS method. For pure Fe samples, concentration of the iron ions in the electrolyte solution can be used to determine the quantity of iron that has been removed from the sample due to the corrosion process. The mass loss method (Equation 1) can then be used to calculate the degradation rate. The degradation rate of each sample are listed in Table 11.

Table 11: Degradation rate computed from the *in vitro* degradation products and using the mass lost method for pure iron samples.

Samples	**Immersion time (h)**	**Fe content (mg/l)**	**Mass loss (μg)**	**Degradation rate (mmpy)**
Fe 1	168	20	300	0,125912185
Fe 2	168	16,9	253,5	0,106395797
Fe 3	168	15,5	232,5	0,097581944
Fe 4	168	32,2	483	0,202718619
Fe 5	168	39,2	588	0,246787884
Fe 6	24	0,54	8,1	0,023797403
Fe 7	24	0,52	7,8	0,022916018
Fe 8	24	0,56	8,4	0,024678788
Fe 9	24	0,97	14,55	0,042747187
Fe 10	24	0,6	9	0,026441559
Fe 11	5	0,11	1,65	0,023268572
Fe 12	5	0,09	1,35	0,019037922
Fe 13	5	0,12	1,8	0,025383897
Fe 14	5	0,18	2,7	0,038075845
Fe 15	5	0,1	1,5	0,021153247

The same method was used to evaluate the corrosion rate from the *in vitro* degradation products for the TWIP samples. To calculate the mass loss, both iron and manganese ions concentrations were used. Data can be found in Table 12. However, only 5 samples were available and consequently, the corrosion rate was only calculated after 5 hours.

Table 12: Degradation rate computed from the *in vitro* degradation products ans using the mass lost method for TWIP samples.

Samples	**Immersion time (h)**	**Fe content (mg/l)**	**Mn content (mg/l)**	**Mass loss (μg)**	**Degradation rate (mmpy)**
TWIP 1	5	2,81	0,94	56,25	0,611136891
TWIP 2	5	3,9	1,22	76,8	0,836259804
TWIP 3	5	0,79	0,47	18,9	0,212894805
TWIP 4	5	4,7	1,45	92,25	1,075417609
TWIP 5	5	1,52	0,6	31,8	0,370713062

In Figure 16, means and standard deviations for each immersion time and for both materials are plotted. The effect of exposure time can be clearly observed for the pure Fe samples but not for the TWIP samples since their number was limited. For iron samples, no significant difference was observed between 5 and 24 hours (p-value = 0,4206). However, between 24 and 168 hours, a significant acceleration (p-value = 0,0079) in the degradation rate can be seen. This is desirable for a candidate material for biodegradable stent application.

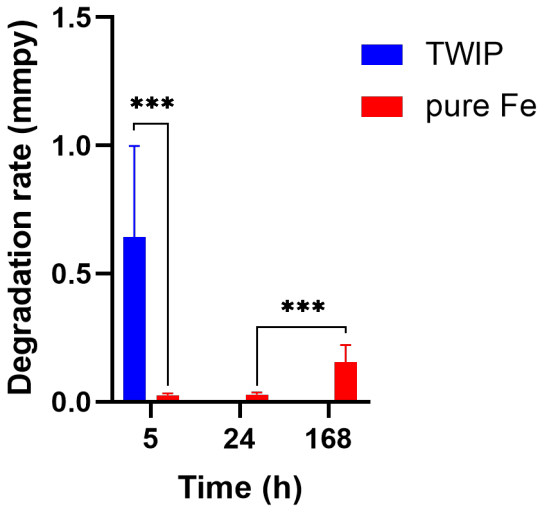

Figure 16: Degradation rate for TWIP and pure Fe samples using ICP-MS (n=5 per condition).

The degradation rate of TWIP is also significantly higher than the one of pure iron after 5 hours (p-value = 0,0046). This means that the corrosion rate has been significantly improved. However, this is not specifically due to the composition of the alloy. The two samples have different shapes, which can have an impact on the degradation rate. According to Milheiro *et al.*, who have compared the different degradation rates of palladium-based alloys using ICP-MS, the shape of the specimens can considerably influence the metal ions release [81]. This could also be the case between TWIP and pure iron and more research should be done to confirm this assumption. Also, roughness can have a significant impact on the rate of degradation. Hilbert *et al.* have proven that the corrosion resistance can be improved by smoothing the surface of a material [82].

Unfortunately due to the limited sample availability, no conclusion can be drawn about the acceleration of the corrosion rate of TWIP over time. A protective layer may form and prevent further corrosion. It was the case in a study carried out by Hermawan *et al.* where the corrosion of pure iron, pure magnesium and alloys with different composition was analyzed using 3 different test setups. Fe-35Mn, a Fe-based alloy containing 35 at.% Mn, showed a decreased corrosion rate due to the precipitation of a protective layer containing calcium and phosphor that inhibited further corrosion. The same precipitation was also found on iron, but it did not inhibit the corrosion reaction so well, as it did not form a continuous layer [61]. This observation is based on a static immersion test filled with Hank's solution so, the setup was not the same as the one used in the experiment for this master thesis. Since the *in vitro* degradation products give no information on the

composition of the samples surface, no conclusion can be drawned about the formation or not of a protective layer preventing further corrosion. However, before selecting TWIP as a potential candidate for biodegradable stent applications, further studies should be carried out to better understand the corrosion and its behaviour over time.

2.1.2 MicroCT-based degradation rate

MicroCT imaging allowed to visually observe wether a material has undergone corrosion during its immersion. On Figure 17, the corrosion is quite visible, both for pure Fe and TWIP, even after 5 hours of immersion. However, CTVox (Bruker) does not allow for doing any quantitative analysis [75].

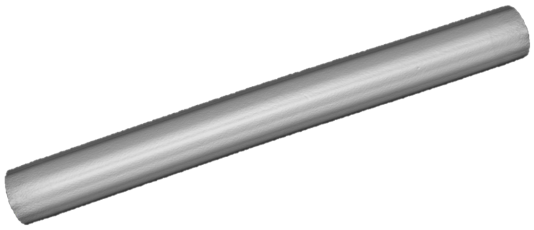

(a) Pure Fe (sample 15) before immersion.

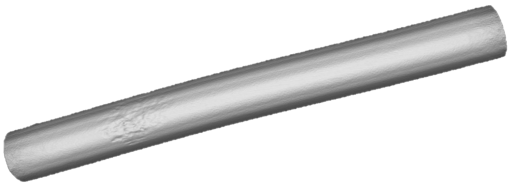

(b) Pure Fe (sample 15) after 5 hours of immersion.

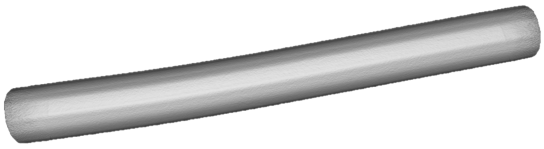

(c) Pure Fe (sample 8) before immersion.

(d) Pure Fe (sample 8) after 24 hours of immersion.

(e) Pure Fe (sample 1) before immersion.

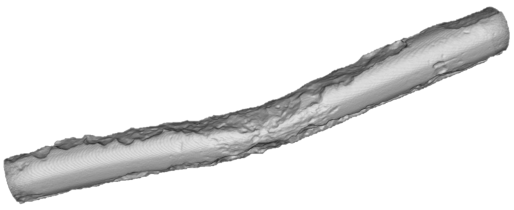

(f) Pure Fe (sample 1) after 7 days of immersion.

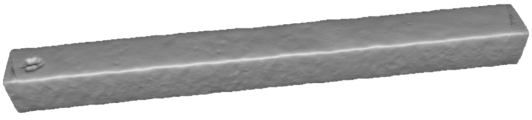

(g) TWIP (sample 2) before immersion.

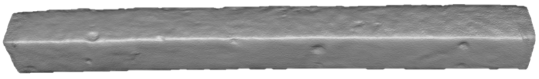

(h) TWIP (sample 2) after 5 hours of immersion.

Figure 17: Visual degradations of Pure Fe and TWIP samples using CTVox and after different times of immersion.

A quantitative analysis can be done by measuring the volume of each sample prior to and after immersion. This was done to evaluate the corrosion rate. By knowing the density of the material and the volume difference before and after immersion, the mass loss can be calculated. Degradation rates were evaluated using this method and data is listed in Table 13.

Table 13: MicroCT-based degradation rate measured using the mass lost method for pure Fe samples (2394 images); n=5 per condition.

Samples	**Immersion time (h)**	**Initial volume (mm^3)**	**Final volume (mm^3)**	**Mass loss (μg)**	**Degradation rate (mmpy)**
Fe 1	168	0,12506	0,10748	138,179	0,487528117
Fe 2	168	0,12658	0,10367	180,073	0,635339543
Fe 3	168	0,12638	0,11242	109,726	0,387138368
Fe 4	168	0,12761	0,12611	11,79	0,041597962
Fe 5	168	0,12843	0,11766	84,6522	0,298673369
Fe 6	24	0,12745	0,12911	-13,0476	-
Fe 7	24	0,12703	0,12987	-22,3224	-
Fe 8	24	0,12659	0,12745	-6,7596	-
Fe 9	24	0,12618	0,13085	-36,7062	-
Fe 10	24	0,12778	0,12898	-9,432	-
Fe 11	5	0,12604	0,12812	-16,3488	-
Fe 12	5	0,12612	0,12756	-10,7682	-
Fe 13	5	0,12642	0,12501	11,0826	1,313830038
Fe 14	5	0,12618	0,12971	-27,7458	-
Fe 15	5	0,12677	0,12882	-16,113	-

Many mass losses are negative, which means that the volume after immersion is greater than the one before immersion. This could be due to some aliasing effect (Figure 18) on top and at the bottom of the wires. To verify this assumption, only the 1000 central images were considered and the degradation rate was calculated based on them (Table 14).

(a) First bottom image of a pure Fe wire. (b) Binary image.

Figure 18: Aliasing effect

Table 14: MicroCT based degradation rate measured using the mass lost method for pure Fe samples (1000 images); n=5 per condition.

Samples	**Immersion time (h)**	**Initial volume (mm^3)**	**Final volume (mm^3)**	**Mass loss (μg)**	**Degradation rate (mmpy)**
Fe 1	168	0,05228	0,04148	84,888	0,716299456
Fe 2	168	0,05282	0,04201	84,966	0,716962696
Fe 3	168	0,05287	0,04492	62,487	0,527275988
Fe 4	168	0,05331	0,05352	-1,6506	-
Fe 5	168	0,05374	0,0505	25,4664	0,214889837
Fe 6	24	0,05323	0,05388	-5,109	-
Fe 7	24	0,05313	0,05429	-9,1176	-
Fe 8	24	0,05292	0,05289	0,2358	0,013928045
Fe 9	24	0,0527	0,05483	-16,7418	-
Fe 10	24	0,05342	0,05383	-3,2226	-
Fe 11	5	0,05265	0,05359	-7,3884	-
Fe 12	5	0,05273	0,05332	-4,6374	-
Fe 13	5	0,05286	0,05223	4,9518	1,403946933
Fe 14	5	0,05273	0,05463	-14,934	-
Fe 15	5	0,05297	0,05385	-6,9168	-

Again, several mass losses are negative, which means that there are other reasons for the increase in the volume of the wires after their immersion. Three additional assumptions can be made :

1. Only the central 2394 μm of the wires were scanned by MicroCT. It is possible that, during the immersion, wires were curved due to the corrosion process. If it is the case, then the volume after immersion can become greater than the volume before immersion. On Figure 19, one can guess that the pure Fe wire is a little bit more curved after immersion than before it.

(a) Before immersion (V1). (b) After immersion (V2).

Figure 19: Schematic representaiton of the curvature of a cylindrical sample before and after immersion; V1<V2.

2. An other reason for the increase in the volume may be the formation of a protec-

tive layer on the surface of the sample. The same assumption was made for results obtained with ICP-MS. This protective layer can, on the one hand, increase the volume of the samples and, on the other, inhibit further corrosion. Both will contribute to a decreased mass loss of the samples. Analysis of the scans has allowed us to observe the possible presence of a protective layer (brighter regions on Figure 20). To verify that this assumption is correct, more research on the corrosion mechanism and analysis of the samples surface composition should be done.

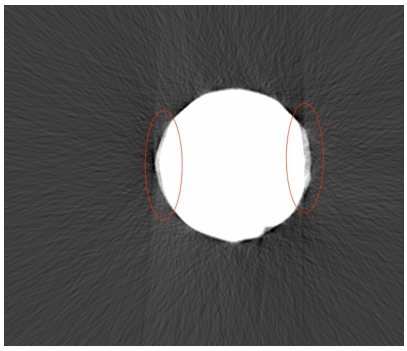

Figure 20: Presence of a protective layer on a pure Fe sample (sample 8) after 24 hours of immersion.

3. The results of ICP-MS show that the change in mass loss compared to the total mass of the samples (about 8 mg) is extremely small, i.e. just a few micrograms. The spatial resolution of the images is maybe just not high enough and the software is not able to detect such small differences. If we do a quick calculation :

$$1 \text{ voxel} = 1\ \mu\text{m}^3$$

The smallest mass loss calculated from ICP-MS data was about 1,3 μg, which corresponds to the volume of 0,000165 mm^3 or 165 000 voxels. For microCT, the mass loss was computed on a much smaller region (about 8 time smaller). Therefore, the difference in volume is expected to be very small (about 168 000 divided by 8 or 21 000 voxels). A scanned wire is composed of about $5\text{x}10^7$ voxels. Hence, the change in weight (and volume) is so small, that the resolution of the CT might not be sufficient to capture this difference.

Finally, when comparing the microCT-based degradation rates obtained after 168 hours of immersion between 2394 and 1000 images, no significant difference is observed (p-value = 0,2581). This suggests that the central part of the wire has not undergone higher corrosion than its ends. Therefore, the corrosion uniformity assumption that was made to decrease the size of the scanned sample can be confirmed with more certainty. No comparison could be done after 5 and 24 hours because of the negative values.

The same procedure was used to analyse the degradation rate of TWIP samples. Results are listed in Table 15.

Table 15: MicroCT-based degradation rate computed using the mass loss method for TWIP samples (2394 images); n=5 per condition.

Samples	**Immersion time (h)**	**Initial volume (mm^3)**	**Final volume (mm^3)**	**Mass loss (g)**	**Degradation rate (mmpy)**
TWIP 1	5	0,12249	0,12197	3,88321	0,42189732
TWIP 2	5	0,12141	0,12595	-33,9034	-
TWIP 3	5	0,11475	0,11346	9,63335	1,08512661
TWIP 4	5	0,13395	0,13777	-28,5267	-
TWIP 5	5	0,11518	0,11381	10,2308	1,13161006

Again, it was observed that some mass losses were negative. Therefore, only the 1000 central images were considered and results are displayed in Table 16.

Table 16: MicroCT-based degradation rate computed and using the mass loss method for TWIP samples (1000 images); n=5 per condition.

Samples	**Immersion time (h)**	**Initial volume (mm^3)**	**Final volume (mm^3)**	**Mass loss (g)**	**Degradation rate (mmpy)**
TWIP 1	5	0,05141	0,05111	0,00000224031	0,525074925
TWIP 2	5	0,05045	0,05202	-0,0000117243	-
TWIP 3	5	0,0483	0,04802	0,00000209096	0,49006993
TWIP 4	5	0,0563	0,05792	-0,0000120977	-
TWIP 5	5	0,04853	0,04729	0,00000925996	2,17030969

The removal of some superior and inferior layers did not give better results and some negative mass losses were still present. To explain those results, the assumptions made for pure Fe are also valid. A surface analysis of the sample after immersion should be done to confirm the second one.

Finally, no significant difference (p-value = 0,75) was observed between degradation rates measured on 2394 and 1000 images. Again, this means that the corrosion is homogeneous on this part of the wire.

No comparison could be made between the degradation rate of pure Fe and TWIP using microCT since most of the data is negative for pure Fe after 5 hours.

2.1.3 Correlation ICP-MS versus MicroCT

Depending on the method, measurements have been done on different lengths :

- ICP-MS was done on the total length of the wires, i.e. 2 cm
- MicroCT (2394 images) was done on the total scanned length, i.e. 0,2394 cm
- MicroCT (1000 images) was done on the 1000 central images, i.e. 0,1 cm

Therefore, the correlation between ICP-MS- and microCT-based degradation rate after 7 days was computed to confirm the assumption of homogeneity of the degradation rate for pure Fe (Figure 21) and TWIP samples (Figure 22b).

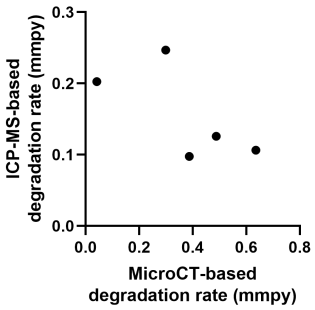

(a) r = -0,678

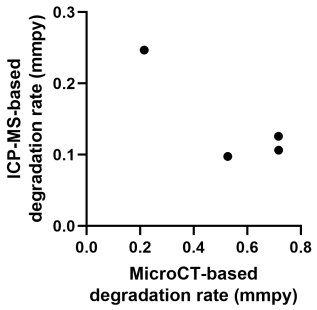

(b) r = -0,8653

Figure 21: Correlation between ICP-MS- and microCT-based degradation rates for pure Fe samples. Left : microCT (2394 images); right : microCT (1000 images).

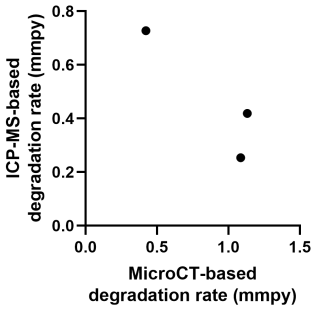

(a) r = -0,9174

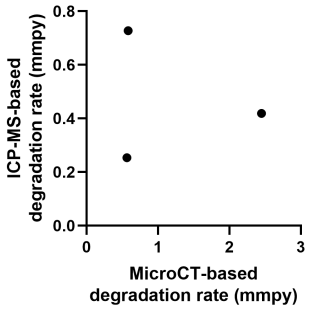

(b) r = -0,1636

Figure 22: Correlation between ICP-MS- and microCT-based degradation rates for TWIP samples. Left : microCT (2394 images); right : microCT (1000 images).

The correlation between ICP-MS- and microCT-based degradation rates is not significant in both cases and for both materials, which may indicate an heterogeneity in the degradation rate. However, microCT has shown many limitations which have surely impacted the computation of the mass loss. Therefore, the main reason for this poor correlation is more likely to be due to the measurement methods themselves than the heterogeneity in the degradation rate.

2.1.4 General discussion

The degradation rate of pure Fe and TWIP samples was evaluated using two different techniques. For each of them, the mass loss was measured. ICP-MS has allowed us to observe the effect of immersion time. There was a difference in corrosion rate between 5, 24 and 168 hours of exposure time. ICP-MS has also enabled the evaluation of the differences in corrosion rate between pure Fe and TWIP. The degradation rate of TWIP was significantly higher. However, alloying is maybe not the only reason for this improvement. Shape as well as initial roughness can also have an influence on the degradation

rate. ICP-MS could not provide any information on this. Moreover, variation of the degradation rate of TWIP over time could not be assessed since only 5 samples were available.

MicroCT showed many limitations for the calculation of the degradation rate of pure Fe and TWIP. Therefore, the results are not really meaningful for the analysis of the degradation rate. However, visualization of the scans has allowed us to observe the presence of a possible protective layer. To confirm this assumption, more studies should be conducted to look into the composition of the samples surface.

2.2 Roughness

Roughness is considered to have an important influence on stent performance. Indeed, while smooth surface stents were previously associated with reduced thrombogenicity and neointimal proliferation, more recent experimental studies have suggested that stents with a previously treated rough surface may accelerate endothelialization. The storage capacity of anti-restenotic drugs can also be improved due to the roughness present on the surface of the stent. Moreover, an accurate evalution of the surface roughness can help analyse the local mechanical and dynamic properties of fluids, which are known to have an influence on ISR.

In the case of biodegradable stents, surface roughness is expected to vary during degradation. Therefore, monitoring roughness parameters during *in vitro* degradation is useful to estimate the modifications in surface topography and its consequences that a stent would undergo *in vivo*.

In order to set-up a robust characterization protocol for roughness measurements of stents, we have assessed different analysis protocols.

2.2.1 Influence of the number of profile lines per sample

To see if the number of profile lines could have an influence on the roughness values, comparison was made between 16 and 8 measurements per sample. It was expected that this comparison would help us assess the homogeneity of the roughness around the sample as well. To see if the difference was significant, non parametric paired student t-tests were performed and the p-values were calculated for each material after immersion. This was done on all the data collected with both Matlab routines. "Short" and "long" stand for data collected with code 1 for a length of 2394 μm and 798 μm respectively, and "curved" stands for data collected with code 2 on 2394 μm of length.

No significant differences were found, which may indicate an homogeneous corrosion around the wires. However, when plotting the individual points for 2 different samples after 24 hours of immersion, the presence of outliers is clearly visible, which indicates the presence of pitting corrosion or any other local corrosion (Figure 25).

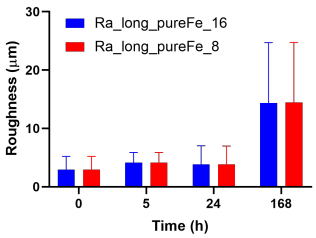

(a) R_a from long measurements and using code 1.

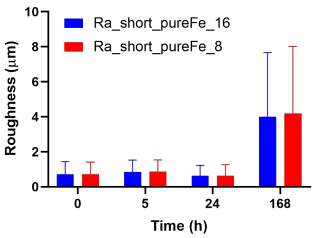

(b) R_a from short measurements and using code 1.

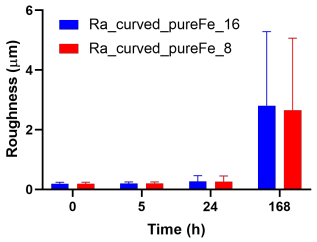

(c) R_a from long measurements and using code 2.

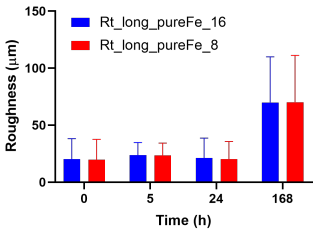

(d) R_t from long measurements and using code 1.

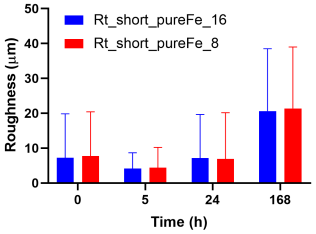

(e) R_t from short measurements and using code 1.

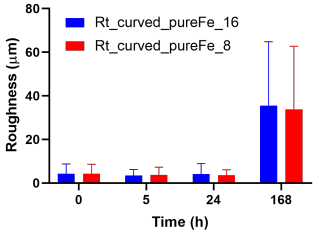

(f) R_t from long measurements and using code 2.

Figure 23: Comparison of the number of profile lines (8 and 16) for pure Fe samples.

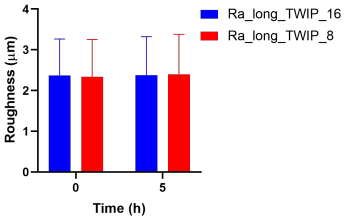

(a) R_a from long measurements and using code 1.

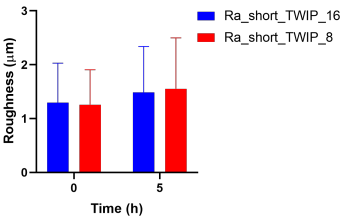

(b) R_a from short measurements and using code 1.

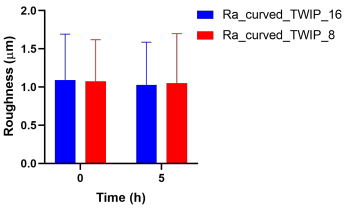

(c) R_a from long measurements and using code 2.

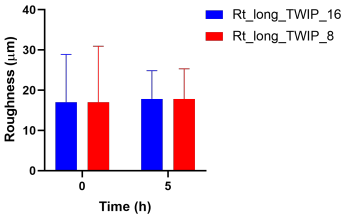

(d) R_t from long measurements and using code 1.

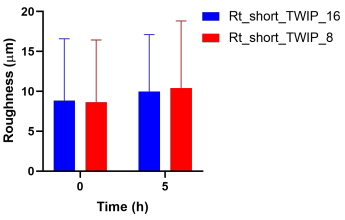

(e) R_t from short measurements and using code 1.

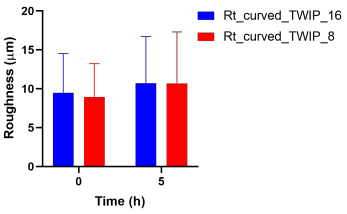

(f) R_t from long measurements and using code 2.

Figure 24: Comparison of the number of profile lines (8 and 16) for TWIP samples.

(a) Sample 7 (b) Sample 10

Figure 25: Analysis of the presence of outliers for R_t after 24 hours of immersion for long measurements and using code 1. Each point corresponds to one measurement.

For sample 10 (Figure 25b), the outliers are still present for 8 measurements but for sample 7 (Figure 25a), this information is lost when the number of measures is divided by two thereby reducing the average roughness. However, despite local pitting, and limited general effect of the corrosion on the surface, similar average roughness and standard deviations are still obtained as shwon in Figure 23 and 24 . Therefore, in case of outliers (indicating the presence of pits), they can easily be missed if the number of profile lines is too low. That is why, the rest of the analysis will be based on values obtained with 16 measurements. However, maybe more measurements are needed to take fully into account the homogeneities.

2.2.2 Homogeneity of the roughness

To be a potential candidate for biodegradable stents, the investigated material should degrade uniformly. So far, no tool allows for the analysis the roughness in 3D. Therefore, multiple 2D analyses of the roughness along and around the sample may help evaluate the uniformity both of the roughness and degradation. Uniformity of the roughness around the sample was investigated in section 2.2.1. by evaluating the roughness with different numbers of profile lines. The assumption of uniformity around the sample could not be confirmed since the presence of outliers was found on different samples. To further assess the homogeneity of the roughness along the samples, measurements on smaller and larger ROIs were done (Figure 29). Small length measurements were done on the upper region of the samples and their length was equal to 798 μm. Large length measurements were done on the total length of the samples to comply with ISO standards as much as possible ISO [77]. Means were then compared with non parametric student t-tests.

We found significant differences for all time points, and for both materials. This may indicate a heterogeneity in the roughness along the samples. However, before making this assumption, it should be remembered that the code used to make the measurements (code 1) does not take into account the waviness of the samples. Therefore, this increase in the roughness may also be due to the waviness of the samples, which are seldom perfectly straight. Samples can be curved (Figure 15) meaning that the distance between the green line and the red line is higher in the middle of the wires than it is at their ends. Again,

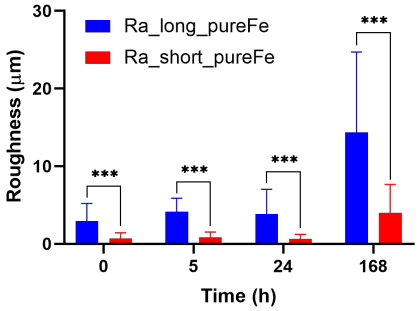

(a) R_a for long and short measurements

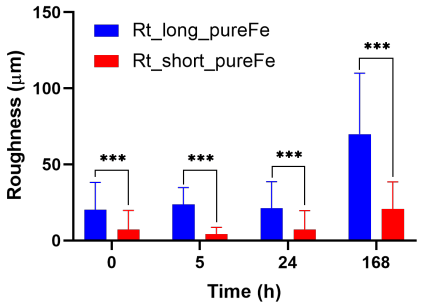

(b) R_t for long and short measurements

Figure 26: Homogeneity of the roughness for pure Fe samples

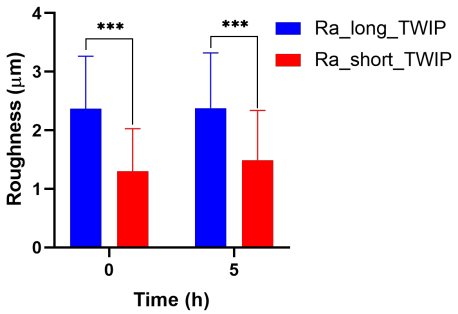

(a) R_a for long and short measurements

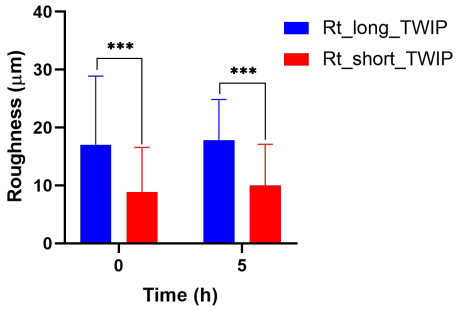

(b) R_t for long and short measurements

Figure 27: Homogeneity of the roughness for TWIP samples.

no conclusion can be drawn regarding the homogeneity along the sample because of the limitations of code 1. Further analysis should be conducted with more adapted codes such as code 2 or the third one that is able to create polygonal baselines.

2.2.3 Comparison of the Matlab routines

The first Matlab routine (code 1) can only measure roughness on straight surfaces. During degradation and samples handling, the curvature of the wire can vary. Even before degradation, wires can be curved. This can lead to roughness overestimation. To deal with curved surfaces, code 1 was adapted and improved. A new code was created (code 2), which has allowed us to select multiple points on the surface analysed (8 in our case). Between each point, a linear baseline is created allowing us to follow the curvature of the wire. To compare code 1 and code 2, non parametric students t-tests were performed and again, p-values were computed.

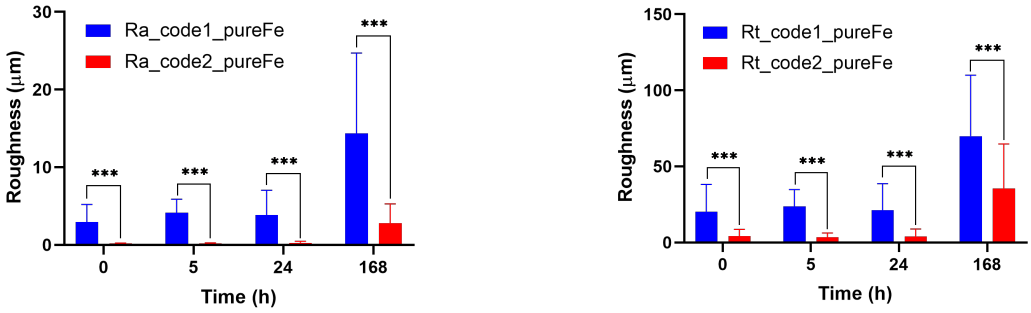

(a) (b)

Figure 28: Comparison of Matlab routines for Pure Fe samples (left : R_a, right : R_t). Code 1 = Computation of roughness parameters with one linear baseline; code 2 = Computation of roughness parameters with multiple linear baselines.

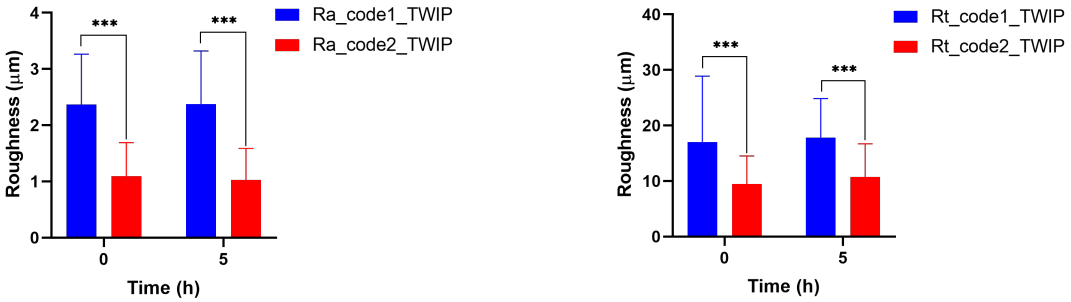

(a) (b)

Figure 29: Comparison of Matlab routines for TWIP samples (right : R_a, left : R_t). Code 1 = Computation of roughness parameters with one linear baseline; code 2 = Computation of roughness parameters with multiple linear baselines.

For both materials and for every time point, roughness parameters were significantly lower for code 2 (pvalues $<$ 0,0001). The main explanation for this is the inability of code 1 to take into account the waviness and the curvature of the wire. As shown in Figure 15, this

results in roughness overestimation, which highly limits the use of code 1 to estimate the roughness parameters. Indeed, having a perfectly flat surface is almost impossible. Code 2 seems to be more adapted for roughness evaluation. However, it still has some limitations as measurements are also based on linear baselines. Waviness is indeed rarely composed of a unique wavelength but rather of multiple different wavelengths. As a result, linear baselines would never be able to perfectly take into account the waviness of the profile.

A third code has been created to overcome those limitations where linear baselines are replaced by polygonal baselines. Further analysis of the roughness should be done using this code and comparison should be made with the two other codes.

Also, the validity of high-resolution microCT potential for the quantification of the roughness needs to be assessed by comparing results obtained with microCT and standard profile measuring systems such as optical or contact profilometry. Indeed, Kerckhofs *et al.* have shown that for high roughness (micro-scale) surfaces, a microCT-based protocol could be used with comparable or even better accuracy than standard profile measuring systems. But for small roughness (submicron-scale), since the spatial image resolution is equal to 1 μm, the microCT protocol could overestimate the roughness paramters [39]. So, before drawing any conclusions, more studies should be conducted to evaluate roughness parameters using microCT as well as standard techniques.

In the rest of this thesis, analysis will only be made using roughness parameters obtained with code 2, which is considered more relevant.

2.2.4 Variation of the roughness over time

Roughness is expected to vary during degradation. To analyse the magnitude of this variation, surface roughness was measured after three different periods of immersion : 5 hours, 24 hours and 7 days for pure Fe (Figure 30) and only after 5 hours for TWIP (Figure 31). Parameters such as R_a and R_t were evaluated and non parametric student t-tests were performed. This was done based on data collected with code 2.

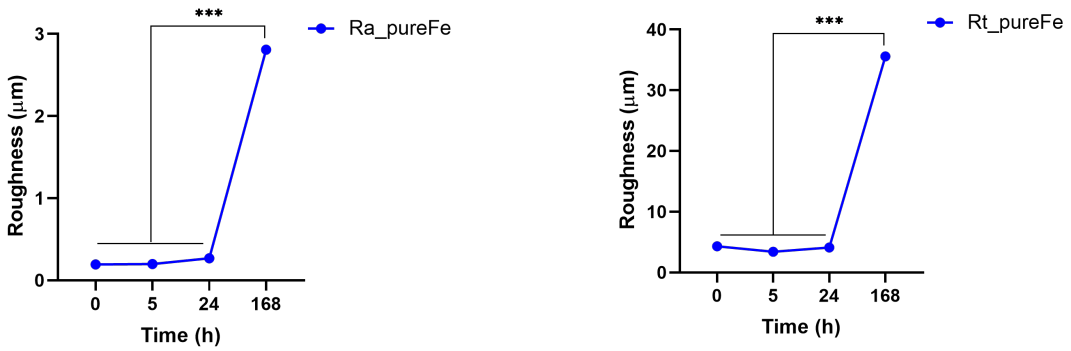

(a) (b)

Figure 30: Variation of the roughness with time for pure Fe samples (left = R_a; right = R_t).

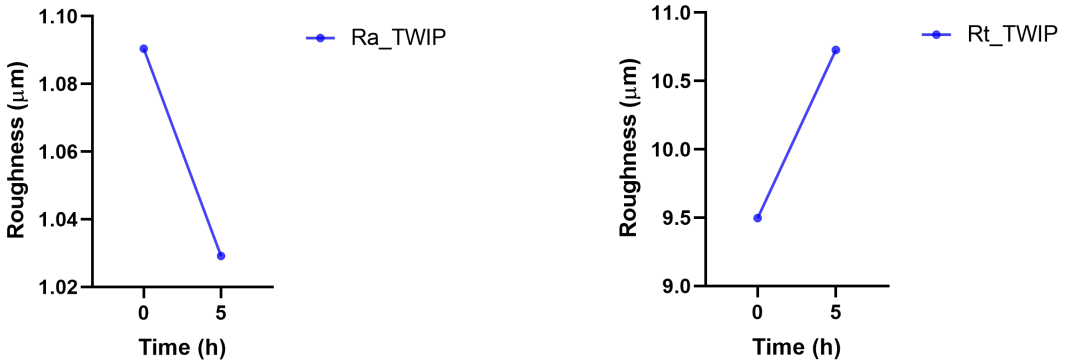

(a) (b)

Figure 31: Variation of the roughness with time for TWIP samples (left = R_a; right = R_t).

For pure Fe samples, the difference after 5 hours and 24 hours compared to prior immersion is not significant for both roughness parameters. It only becomes significantly higher after 7 days of immersion. For TWIP samples, no significant difference was observed after 5 hours compared to prior immersion

2.2.5 Comparison of the roughness of TWIP and pure Fe

Since the roughness of TWIP wires was only assessed after 5 hours of immersion, the comparison between pure Fe and TWIP was made before immersion and only for this time point (Figure 32).

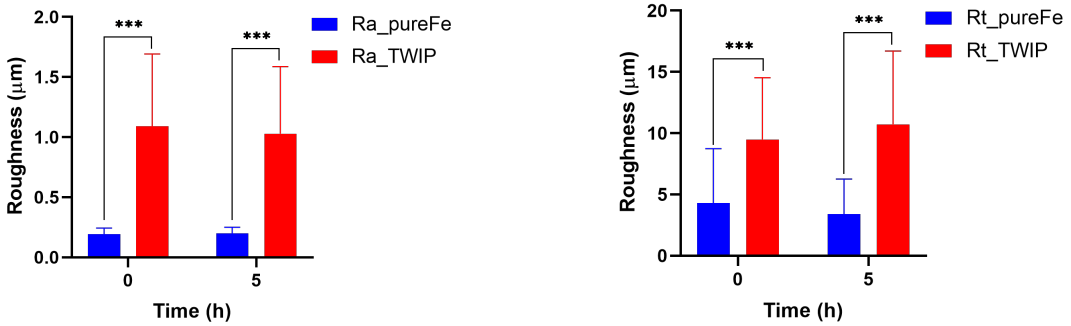

(a) (b)

Figure 32: Comparison of TWIP and pure Fe roughness parameters before and after 5 hours of immersion (left = R_a; right = R_t).

The roughness of TWIP is significantly higher prior to and after 5 hours of immersion than it is for pure Fe. The higher initial roughness of TWIP is caused by the manufacturing process. Indeed, the pure iron wires were bought commercially while the TWIP wires were manufactured in-house. The roughness of TWIP is significantly higher because of the defects that appeared on the surface when the metal were cut to make the wires.

However, the change in roughness for pure Fe and TWIP between before and after 5 hours immersion might be the same. To analyse this, absolute and relative changes for

R_a and R_t were computed (Table 17). After 5 hours of immersion, the relative change for R_a is negative for both materials, meaning a decreased roughness. This decrease is higher for pure Fe samples. When making 2D measurements, 2D cross-sectional images are randomly selected on the sample, which means that outliers found prior to immersion could not be included after immersion anymore. So, this decrease may highlighted the limitations of 2D measurements and the need for 3D measurements. For R_t, the relative change is a little bit higher for TWIP, meaning that the roughness increases faster for TWIP. However, this parameter is only representative of the "extremes" values and not the global roughness. Therefore, this could indicate higher local corrosion for TWIP.

Table 17: Absolute and relative roughness changes for TWIP and pure Fe samples.

		Absolute change (μm)			**Relative change (%)**		
		t0-t5	t5-t24	t24-t168	t0-t5	t5-t24	t24-t168
Pure Fe	R_t	0,0057	0,0692	2,5403	2,967	34,707	945,654
	R_a	-0,9035	0,7112	31,4446	-20,941	20,85	762,77
TWIP	R_t	0,0612	-	-	5,615	-	-
	R_a	-1,2309	-	-	-0,129	-	-

2.2.6 Influence of the roughness on the degradation rate

TWIP samples have shown faster degradation than that of pure Fe samples. According to the literature, initial roughness can have a significant impact on the degradation rate [82]. To verify this assumption, correlation between initial roughness and degradation rate calculated from ICP-MS results was analysed for both samples, using R_a. For measurements made with code 2, and because both the initial roughness and the degradation rate after 5 hours of immersion were higher for TWIP than for pure Fe, a correlation between them was possible.

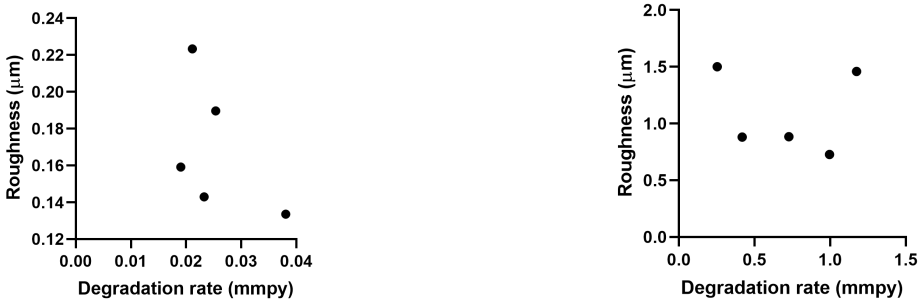

(a) r = -0,5113 (b) r = -0,1112

Figure 33: Correlation between initial R_a and the degradation rate computed with ICP-MS after 5 hours of immersion (left = pure Fe; right = TWIP)

For both materials, a low correlation was found between the initial roughness and the degradation rate. As a result, it may be assumed that alloying has effectively improved the degradation of pure Fe samples and that the increase was not due to an initial higher roughness. To confirm this, studies should be conducted to analyse the influence of the shape.

2.2.7 General discussion

MicroCT seems to be more promising to compute the roughness than the degradation rate of candidate materials for stent applications. Code 1 has shown many limitations since it was not able to take into account the curvature of the wire. Therefore, the homogeneity assumption of the roughness along the samples could not be confirmed. However, code 2 enabled us to observe the presence of outliers, meaning that both pure Fe and TWIP samples have undergone pitting corrosion, which is undesirable. It also allowed us to estimate the roughness evolution over time for pure Fe samples, to compare pure Fe and TWIP roughness and to calculate the correlation between the initial roughness and the degradation rate. This correlation enabled us to confirm that the degradation rate of TWIP was effectively increased by alloying and not because of a higher initial roughness.

However, the ability of microCT to evaluate the roughness needs to be confirmed by comparing microCT and standards profile measurement systems results.

Part V
Conclusion and perspectives

The main goal of this work was to assess and optimise the microCT-based protocol for roughness and degradation rate evaluation. For this purpose, we used and compared both physical measurements, as well as microCT-based measurements; the latter being new in the field. To gather the data, the corrosion rate and roughness evolution of TWIP and pure iron were evaluated during in *in vitro* immersion.

The first section of this work consisted of the assessment and the analysis of the degradation rate. For this purpose, two methods have been used : ICP-MS and microCT. MicroCT has highlighted several limitations and the results could not give us clear insights into the evolution of the degradation rate for both materials over time. However, it has enabled us to observe the presence of brighter regions on the scans, which may suggest that a protective layer on the samples surface has formed. ICP-MS has allowed us to acquire quantitative data on the degradation rate. A significantly higher degradation rate was observed for the TWIP samples. Finally, no information regarding the corrosion mechanism with ICP-MS was found. Going forward, analysis of the components of the surface should be made to confirm the assumption of the presence of a protective layer. Also, to better observe the effect of exposure time on the materials, experiments should be carried out with more time points. Obviously, more TWIP samples should be produced. To determine what the factors influencing the degradation rate are, samples should have different shapes and initial levels of roughness. Last but not least, *in vitro* and *in vivo* experiments should be correlated to be able to assess the effeciency of the dynamic immersion test used in this master thesis and its ability to mimic, as much as possible, the *in vivo* conditions.

The second section of this thesis focused on the analysis of the roughness and its variation over time. Two different Matlab routines have been used to evaluate the roughness parameters. Both have highlighted limitations because of the use of linear baselines instead of polygonal baselines. Furthermore, they only allow for multiple 2D measurements, which can be time consuming. Even though it was expected that selecting 16 different 2D cross-sectional images could give us a good overview of the roughness in 3D, outliers were identified during the analysis. We found that this information can be lost if the outliers are not present on the 2D cross-sectional images. Moreover, images were randomly selected on the sample, which means that outliers found prior to immersion could not be included after immersion anymore. Consequently, a solution should be found to make sure that the roughness is systematically analysed on the same part of the wire. Moreover, additional work should be done to evaluate the roughness with polygonal baselines. Ideally, the roughness should be analysed with a routine that could compute the roughness parameters in 3D, taking into account any outliers. Measurements should also be made using more time points, especially for TWIP, in order to better observe the variation of the roughness over time. Finally, measurements should be made using standard profile measuring systems such as optical or contact profilometry. Indeed, the submicron-scale roughness evaluated with the microCT-based protocol can be overestimated. Therefore, the results obtained both with microCT and standard profile measuring systems should be compared.

References

[1] World Health Organization. https://www.who.int/news-room/fact-sheets/detail/cardiovascular-diseases-(cvds). Accessed on 3/04/20.

[2] Institute of Medicine, Board on the Health of Select Populations, and Committee on Social Security Cardiovascular Disability Criteria. *Cardiovascular Disability: Updating the Social Security Listings*. The National Academies Press, Washington, D.C., 2010.

[3] Heart and Stroke. https://www.heartandstroke.ca/heart/conditions/coronary-artery-disease. Accessed on 3/04/20.

[4] National Heart Lung and Blood Institute. https://www.nhlbi.nih.gov/health-topics/stents. Accessed on 3/04/20.

[5] Marc Vorpahl, Jason R Foerst, Malte Kelm, Aaron V Kaplan, Renu Virmani1, and Timothy Ball. The complementary role of microCT and histopathology in characterizing the natural history of stented arteries. *Expert Review of Cardiovascular Therapy, 9(7):939–948, 2011.*

[6] Maryam Moravej and Diego Mantovani. Biodegradable Metals for Cardiovascular Stent Application: Interests and New Opportunities. *International Journal of Molecular Sciences, 12:4250–4270, 2011.*

[7] H. Eltchaninoff, C. Tron, L. Sebagh, and A. Cribier. Treatment of intrastent restenosis. *Pathologie Biologie, 52:218–222, 2004.*

[8] Formaggia Luca, Quarteroni Alfio, and Veneziani Alessandro. *Cardiovascular Mathematics : Modeling and simulation of the circulatory system*. Springer, 2009.

[9] Bioscience Notes. http://www.biosciencenotes.com/blood-vessels/. Accessed on 1/05/20.

[10] Barbara J. Bain, Imelda Bates, and Michael A. Laffan. *Dacie and Lewis Practical Haematology, 12th Edition*. Elsevier, 2017.

[11] Maria Alejandra Zuluaga Valencia. Methods for automation of vascular lesions detection in computed tomography images. Master's thesis, Université Claude Bernard - Lyon I; Université des Andes, 2011.

[12] Michael Schinhammer, Anja C. Hänzi, Jörg F. Löffler, and Peter J. Uggowitzer. Structures, bioavailability and protective effects against atherosclerosis. *Food and Chemical Toxicology, 113:49–65, 2018.*

[13] Aziz M. and Yadav K.S. Pathogenesis of Atherosclerosis : A Review. *Medical Clinical Reviews, 2:22, 2016.*

[14] Wikipedia. https://en.wikipedia.org/wiki/Atherosclerosis. Accessed on 13/04/20.

[15] Sara Gargiulo, Matteo Gramanzini, and Marcello Mancini. Molecular Imaging of Vulnerable Atherosclerotic Plaques in Animal Models. *International Journal of Molecular Sciences*, *17*:*1–44*, *2016*.

[16] C. McCormick. *Overview of cardiovascular stent designs*. Woodhead Publishing, University of Strathclyde, Glasgow, United Kingdom, 2018.

[17] Kodikara Arachchillaya Saneera Hemantha Kulathilake. Improvment of coronary angiogrpahy for quantitative coronary analysis by using a computer vision technique. Master's thesis, University of Moratuwa, 2017.

[18] Anja C. Hanzi, Isabel Gerber, Michael Schinhammer, Jorg F. Loffler, and Peter J. Uggowitzer. On the in vitro and in vivo degradation performance and biological response of new biodegradable Mg–Y–Zn alloys. *Acta Biomaterialia*, *6*:*1824–1833*, *2010*.

[19] A. Francis, Y. Yang, S. Virtanen, and A. R. Boccaccinier. Iron and iron-based alloys for temporary cardiovascular applications. *Journal of Materials Science: Materials in Medicine*, *26*:*138*, *2010*.

[20] James S. Lowe and Peter G. Anderson. *Stevens Lowe's Human Histology, 4th Edition*. Elsevier, 2015.

[21] Morlacchi Stefano, Keller Brandis, Arcangeli Patrizia, Balzan Marta, Migliavacca Francesco, Dubini Gabriele, Gunn Julian, Arnold Nadine, Narracott Andrew, Evans David, and Lawford Patricia. Hemodynamics and In-stent Restenosis: Micro-CT Images, Histology, and Computer Simulations. *Annals of Biomedical Engineering*, *39(10)*:*2615–2626*, *2011*.

[22] N. Malik, J. Gunn, C. M. Holt, L. Shepherd, S. E. Francis, C. M. H. Newman, D. C. Crossman, and D. C. Cumberland. Intravascular stents: a new technique for tissue processing for histology, immunohistochemistry, and transmission electron microscopy. *Heart*, *80*:*509–516*, *1998*.

[23] Andreas König and Volker Klauss. Virtual histology. *Heart*, *93(8)*:*977–982*, *2007*.

[24] Marc Vorpahl, Jason R Foerst, Malte Kelm, Aaron V Kaplan, Renu Virmani1, and Timothy Ball. The complementary role of microCT and histopathology in characterizing the natural history of stented arteries. *Expert Review of Cardiovascular Therapy*, *9(7)*:*939–948*, *2011*.

[25] AA Postnov, PC D'Haese, E Neven, NM De Clerck, and VP Persy. Possibilities and limits of X-ray microtomography for in vivo and ex vivo detection of vascular calcifications. *The international journal of cardiovascular imaging*, *25(6)*:*615–624*, *2009*.

[26] Hilary E Barrett, John J Mulvihill, Eoghan M Cunnane, and Michael T Walsh. Characterising human atherosclerotic carotid plaque tissue composition and morphology using combined spectroscopic and imaging modalities. *Biomedical engineering online*, *14(1)*:*S5*, *2015*.

[27] Vinay M Pai, Megan Kozlowski, Danielle Donahue, Elishiah Miller, Xianghui Xiao, Marcus Y Chen, Zu-Xi Yu, Patricia Connelly, Kenneth Jeffries, and Han Wen. Coronary artery wall imaging in mice using osmium tetroxide and micro-computed tomography (micro-CT). *Journal of Anatomy*, *220(5)*:*514–524*, *2012*.

[28] Lisa Leyssens, Carole Verhaegen, Sandrine Horman, Pascal Jacques, and Greet Kerckhofs. Optimization of contrast-enhanced micro-ct for characterization of the in vivo behavior of biodegradable metallic intravascular stents. In *CMBBE 2019*, 2019.

[29] Katrien De Clercq, Eleonora Persoons, Tina Napso, Catherine Luyten, Tatjana N. Parac-Vogt, Amanda N. Sferruzzi-Perri, Greet Kerckhofs, and Joris Vriens. High-resolution contrast-enhanced microCT reveals the true three-dimensional morphology of the murine placenta. *PNAS*, *116(28)*:*13927–13936*, *2019*.

[30] Pijush Kundu, Ira Cohen, and David Dowling. *Fluid Mechanics, 5th Edition*. Elsevier, 2011.

[31] Eoghan M Cunnane, John JE Mulvihill, Hilary E Barrett, and Michael T Walsh. Simulation of human atherosclerotic femoral plaque tissue: the influence of plaque material model on numerical results. *Biomedical engineering online*, *14(S1)*:*S7*, *2015*.

[32] C Conway, JP McGarry, and PE McHugh. Modelling of atherosclerotic plaque for use in a computational test-bed for stent angioplasty. *Annals of biomedical engineering*, *42(12)*:*2425–2439*, *2014*.

[33] Elena Z. Golukhovaa, Marina V. Grigoriana, Mariya N. Ryabininaa, Naida I. Bulaevaa, Seth Fortmanna, and Victor L. Serebruanyb. Independent Predictors of Major Adverse Events following Coronary Stenting over 28 Months of Follow-Up. *Cardiology*, *132*:*176–181*, *2015*.

[34] Gong Cheng, Feng jun Chang, Yi Wang, Peng-Hua You, Hai chao Chen, Wen qi Han, Jun wei Wang, Ni er Zhong, and Zhi-qian. Factors Influencing Stent Restenosis After Percutaneous Coronary Intervention in Patients with Coronary Heart Disease: A Clinical Trial Based on 1-Year Follow-Up. *Medical Science Monitor*, *25*:*240–247*, *2019*.

[35] Young Joon Hong, Myung Ho Jeong, Sang Yup Lim, Sang Rok Lee, Kye Hun Kim, Il Suk Sohn, Hyung Wook Park, Ju Han Kim, Weon Kim, Youngkeun Ahn, Jeong Gwan Cho, Jong Chun Park, and Jung Chaee Kang. Elevated Preprocedural High-Sensitivity C-Reactive Protein Levels are Associated With Neointimal Hyperplasia and Restenosis Development After Successful Coronary Artery Stenting. *Circulation Journal*, *69*:*1477 – 1483*, *2005*.

[36] Giuseppe De Luca, Harry Suryapranata, Giovanni Gregorio, Helmut Lange, and Massimo Chiariello. Homocysteine and Its Effects on In-Stent Restenosis. *Circulation*, *112*:*307–311*, *2019*.

[37] Andrew E Ajani, Ron Waksman, Dong-Hun Cha, Luis Gruberg, Lowell F Satler, Augusto D Pichard, and Kenneth M Kent. The impact of lesion length and reference vessel diameter on angiographic restenosis and target vessel revascularization in treating in-stent restenosis with radiation. *Journal of the American College of Cardiology*, *39(8)*:*1290–1296*, *2002*.

[38] Alban Dibra, Adnan Kastrati, Julinda Mehilli, Jurgen Pache, Randolf von Oepen, Josef Dirschinger, and Albert Schomig. Influence of Stent Surface Topography on the Outcomes of Patients Undergoing Coronary Stenting: A Randomized Double-Blind Controlled Trial. *Catheterization and Cardiovascular Interventions*, *65*:*374–380*, *2005*.

[39] Greet Kerckhofs, Grzegorz Pyka, Maarten Moesen, Simon Van Bael, Jan Schrooten, and Martine Wevers. High-Resolution Microfocus X-Ray Computed Tomography for 3D Surface Roughness Measurements of Additive Manufactured Porous Materials. *Advanced engineering materials*, *15(3)*:*153–158*, *2013*.

[40] Zhen Zhen, Ting fei Xi, and Yu feng Zheng. A review on in vitro corrosion performance test of biodegradable metallic materials. *Transactions of Nonferrous Metals Society of China*, *23*:*2283–2293*, *2013*.

[41] Stéphane Cook, Peter Wenaweser, Mario Togni, Cyrill Morger Michael Billinger, Christian Seiler, Rolf Vogel, Otto Hess, Bernhard Meier, and Stephan Windecker. Incomplete Stent Apposition and Very Late Stent Thrombosis After Drug-Eluting Stent Implantation. *Circulation*, *115*:*2426–2434*, *2007*.

[42] Huda Hamid and John Coltart. Miracle stents - a future without restenosis. *Mcgill Journal of Medecine*, *10(2)*:*105–111*, *2010*.

[43] Ae-Young Her and Eun-Seok Shin. Current Management of In-Stent Restenosis. *Korean Circulation Journal*, *48(5)*:*337–349*, *2018*.

[44] Remo Albiero. Cutting Balloon Versus Conventional Balloon Angioplasty for the Treatment of Coronary Artery Disease. *European Cardiology*, *1(1)*:*48–52*, *2005*.

[45] Fernando Alfonso, Robert A.Byrne, Fernando Rivero, and Adnan Kastrati. Current Treatment of In-Stent Restenosis. *Journal of the American College of Cardiology*, *63(24)*:*2659–2673*, *2014*.

[46] Roxana Mehran, George Dangas, Gary S. Mintz, Ron Waksman, Alexandre Abizaid, Lowell F. Satler, Augusto D. Pichard, Kenneth M. Kent, Alexandra J. Lansky, Gregg W. Stone, and Martin B. Leon. Treatment of In-Stent Restenosis With Excimer Laser Coronary Angioplasty Versus Rotational Atherectomy. *Circulation*, *101*:*2484–2489*, *2000*.

[47] George D. Dangas, Bimmer E. Claessen, Adriano Caixeta, Elias A. Sanidas, Gary S. Mintz, and Roxana Mehran. In-Stent Restenosis in the Drug-Eluting Stent Era. *Journal of the American College of Cardiology*, *56(1)*:*897–907*, *2010*.

[48] H. Hermawan, D. Dubé, and D. Mantovani. Developments in metallic biodegradable stents. *Acta Biomaterialia*, *6*:*1693–1697*, *2010*.

[49] M. Moravej, A. Purnama, M. Fiset, J. Couet, and D. Mantovani. Electroformed pure iron as a new biomaterial for degradable stents: In vitro degradation and preliminary cell viability studies. *Acta Biomaterialia*, *6*:*1843–1851*, *2010*.

[50] J. Levesque, D. Dube, M. Fiset, and D. Mantovani. Materials and properties for coronary stents. *Advanced Materials and Processes*, *162(9)*:*45–48*, *2004*.

[51] Li-Da Hou, Zhen Li, Yu Pan, MuhammadIqbal Sabir, Yu-Feng Zheng, and Li Li. Molecular imaging of vulnerable atherosclerotic plaques in animal models. *Frontiers of Materials Science*, *26(3)*:*1–22*, *2016*.

[52] James A. Shand, Adesh Ramsewak, Colm G. Hanratty, Mark S. Spence, and Simon J. Walsh. The concertina effect and the limitations of current drug-eluting stents: is it time to revisit and prioritize stent design over efficacy? *Interventional Cardiology*, *4(3)*:*325–335*, *2012*.

[53] Jaroslav Capek, Kveta Stehlikova, Alena Michalcova, Sarka Msallamova, and Dalibor Vojtech. Microstructure, mechanical and corrosion properties of biodegradable powder metallurgical Fe-2 wt% X (X = Pd, Ag and C) alloys. *Materials Chemistry and Physics*, *181*:*501–511*, *2016*.

[54] Mitsuo Niinomi, Takayuki Narushima, and Masaaki Nakai. *Advances in Metallic Biomaterials: Tissues, Materials and Biological Reactions*. Springer Series in Biomaterials Science and Engineering, 2015.

[55] Zijian Li, Xunan Gu, Siquan Lou, and Yufeng Zheng. The development of binary Mg-Ca alloys for use as biodegradable materials within bone. *Biomaterials*, *29*:*1329–1344*, *2008*.

[56] Sannakaisa Virtanen. Biodegradable Mg and Mg alloys: Corrosion and biocompatibility. *Materials Science and Engineering B*, *176*:*1600–1608*, *2011*.

[57] B. Heublein, R. Rohde, V. Kaese, M. Niemeyer, W. Hartung, and A. Haverich. Biocorrosion of magnesium alloys: a new principle in cardiovascular implant technology? *Heart*, *89*:*651–656*, *2003*.

[58] M. Peuster, P. Wohlsein, M. Brügmann, M. Ehlerding, K. Seidler, C. Fink, H. Brauer, A. Fischer, and G. Hausdorf. A novel approach to temporary stenting : degradable cardiovascular stents produced from corrodible metal - results 6–18 months after implantation into New Zealand white rabbits. *Heart*, *86*:*563–569*, *2001*.

[59] Matthias Peuster, Carola Hesse, Tirza Schloo, Christoph Fink, Philipp Beerbaum, and Christian von Schnakenburg. Long-term biocompatibility of a corrodible peripheral iron stent in the porcine descending aorta. *Biomaterials*, *27*:*4955–4962*, *2006*.

[60] Natalia S. Fagalia, Claudia A. Grilloa, Susana Puntarulob, and Monica A. Fernandez Lorenzo de Melea. Cytotoxicity of corrosion products of degradable Fe-based stents: Relevance of pH and insoluble products. *Colloids and Surfaces B: Biointerfaces*, *128*:*480–488*, *2015*.

[61] H. Hermawan, M. Moravej, D. Dubé, M. Fiset, and D. Mantovani. Degradation Behaviour of Metallic Biomaterials for Degradable Stents. *Advanced Materials Research*, *15-17*:*113–118*, *2007*.

[62] Jaroslav Capek, Sarka Msallamova, Eva Jablonska, Jan Lipov, and Dalibor Vojtech. A novel high-strength and highly corrosive biodegradable Fe-Pd alloy: Structural, mechanical and in vitro corrosion and cytotoxicity study. *Materials Science and Engineering C*, *79*:*550–562*, *2017*.

[63] B. Liu and Y.F. Zheng. Effects of alloying elements (Mn, Co, Al, W, Sn, B, C and S) on biodegradability and in vitro biocompatibility of pure iron. *Acta Biomaterialia*, *7*:*1407–1420*, *2011*.

[64] Michael Schinhammer, Anja C. Hänzi, Jörg F. Löffler, and Peter J. Uggowitzer. Design strategy for biodegradable Fe-based alloys for medical applications. *Acta Biomaterialia*, *6*:*1705–1713*, *2010*.

[65] ASTM F2129-04 : Standard Test Method for Conducting Potentiodynamic Measurements to Determine the Corrosion Susceptibility of Small Implant Devices. Standard, ASTM, 2004.

[66] ASTM G59-97 : Standard Test Method for Conducting Potentiodynamic Polarization Resistance Measurements. Standard, ASTM, 1997.

[67] ASTM G31-99 : Standard Practice for Laboratory Immersion Corrosion Testing of Metals. Standard, ASTM, 1999.

[68] Julie Levesque, Hendra Hermawan, Dominique Dube, and Diego Mantovani. Design of a pseudo-physiological test bench specific to the development of biodegradable metallic biomaterials. *Acta Biomaterialia*, *4*:*284–295*, *1998*.

[69] Myer Kutz. *Handbook of Environmental Degradation of Materials, 2nd Edition*. Elsevier, 2013.

[70] Branko N. Popov. *Corrosion Engineering*. Elsevier, 2015.

[71] Jasbir N. Patel, Andre Chang, Haleh Shahbazbegian, and Bozena Kaminska. Adaptive Corrosion Protection System Using Continuous Corrosion Measurement, Parameter Extraction, and Corrective Loop. *International Journal of Corrosion*, *2016(6)*:*1–11*, *2016*.

[72] N.T. Kirkland, N. Birbilis, and M.P. Staiger. Assessing the corrosion of biodegradable magnesium implants: A critical review of current methodologies and their limitations. *Acta Biomaterialia*, *8*:*925–936*, *2012*.

[73] Léa Paulus. Degradation of biodegradable metallic intravascular stents and roughness analysis. Master's thesis, Université Catholique de Louvain, 2019.

[74] M. Bartosch, H. Peters, A. Koerner, N. Hort, and F. Witte. New methods for in vivo degradation testing of future stent materials. *Materials and Corrosion*, *69*:*156–166*, *2018*.

[75] Bruker. 3D Suite Software. `https://www.bruker.com/products/microtomography/micro-ct-software/3dsuite.html`.

[76] ISO 4287:1997 : Geometrical Product Specifications (GPS). Surface texture : profile method. Terms, definitions and surface texture parameters. Standard, ISO, 1997.

[77] ISO 4288:1996 : Geometrical Product Specifications (GPS). Surface texture : Profile method. Rules and procedures for the assessment of surface texture. Standard, ISO, 1996.

[78] AnaStats. Dixon test. https://www.anastats.fr/telechargements/. Accessed on 12/05/20.

[79] AnaStats. Shapiro & Wilk test. https://www.anastats.fr/telechargements/. Accessed on 12/05/20.

[80] GraphPad Prism 8. https://www.graphpad.com/. Accessed on 5/05/20.

[81] Ana Milheiro, Joris Muris, Cornelis J Kleverlaan, and Albert J Feilzer. Influence of shape and finishing on the corrosion of palladium-based dental alloys. *The journal of advanced prosthodontics*, *7(1)*:*56–61*, *2015*.

[82] Lisbeth R. Hilbert, Dorthe Bagge-Ravn, John Kold, and Lone Gram. Influence of surface roughness of stainless steel on microbial adhesion and corrosion resistance. *International Biodeterioration Biodegradation*, *53*:*175–185*, *2003*.

UNIVERSITÉ CATHOLIQUE DE LOUVAIN
École polytechnique de Louvain
Rue Archimède, 1 bte L6.11.01, 1348 Louvain-la-Neuve, Belgique | **www.uclouvain.be/epl**